nature cancer

Article

https://doi.org/10.1038/s43018-022-00500-z

Targeting T cell checkpoints 41BB and LAG3 and myeloid cell CXCR1/CXCR2 results in antitumor immunity and durable response in pancreatic cancer

Received: 4 August 2022

Accepted: 18 November 2022

Published online: 30 December 2022

Check for updates

Pat Gulhati[1,2], Aislyn Schalck[3], Shan Jiang[4], Xiaoying Shang[4], Chang-Jiun Wu[5], Pingping Hou[4], Sharia Hernandez Ruiz[6], Luisa Solis Soto[6], Edwin Parra[6], Haoqiang Ying[7], Jincheng Han[4], Prasenjit Dey[8], Jun Li[5], Pingna Deng[4], Emi Sei[3], Dean Y. Maeda[9], John A. Zebala[9], Denise J. Spring[4], Michael Kim[3,10], Huamin Wang[11], Anirban Maitra[11], Dirk Moore[12], Karen Clise-Dwyer[13], Y. Alan Wang[4,14,15,16,17] ✉, Nicholas E. Navin[3] & Ronald A. DePinho[4] ✉

Pancreatic ductal adenocarcinoma (PDAC) is considered non-immunogenic, with trials showing its recalcitrance to PD1 and CTLA4 immune checkpoint therapies (ICTs). Here, we sought to systematically characterize the mechanisms underlying *de novo* ICT resistance and to identify effective therapeutic options for PDAC. We report that agonist 41BB and antagonist LAG3 ICT alone and in combination, increased survival and antitumor immunity, characterized by modulating T cell subsets with antitumor activity, increased T cell clonality and diversification, decreased immunosuppressive myeloid cells and increased antigen presentation/decreased immunosuppressive capability of myeloid cells. Translational analyses confirmed the expression of 41BB and LAG3 in human PDAC. Since single and dual ICTs were not curative, T cell-activating ICTs were combined with a CXCR1/2 inhibitor targeting immunosuppressive myeloid cells. Triple therapy resulted in durable complete responses. Given similar profiles in human PDAC and the availability of these agents for clinical testing, our findings provide a testable hypothesis for this lethal disease.

Pancreatic ductal adenocarcinoma (PDAC) is among the most lethal of human cancers, with a 5-year overall survival rate of 11%[1]. Given the rising incidence and minimal change in mortality rates, PDAC is expected to become the second leading cause of cancer deaths by 2030[2,3]. The mainstay of treatment for metastatic PDAC is chemotherapy with gemcitabine- or fluorouracil-based regimens; however, chemotherapy benefit is often modest and transient[2]. While immune checkpoint therapy (ICT) has transformed treatment and survival for numerous advanced cancers, PDAC remains recalcitrant to numerous ICT agents and combinations, including anti-programmed cell death protein 1 (anti-PD-1)/anti-programmed death-ligand 1 (anti-PD-L1), anti-CTLA4 and combined anti-PD-1 and anti-CTLA4 (refs. 4–7).

The lack of response to ICT has been attributed to immunosuppressive conditions in the tumor immune microenvironment (TIME), including prominent myeloid cell infiltration, as well as the scarcity and dysfunction of $CD8^+$ T cells, among others[2,4]. Following chronic antigen

A full list of affiliations appears at the end of the paper. ✉e-mail: yaw@iu.edu; rdepinho@mdanderson.org

exposure in the TIME, $CD8^+$ T cells differentiate into a dysfunctional state characterized by a loss of proliferative capacity and effector functions, as well as expression of inhibitory immune checkpoints, suggesting that these checkpoints may mediate $CD8^+$ T cell exhaustion[2,4]. The functional effects of targeting these immune checkpoints on dysfunctional or exhausted $CD8^+$ T cells in PDAC are currently unknown. Several preclinical and early-phase clinical trials have shown signals of activity with immunotherapy combinations, encouraging further investigation[2,4]. It is tempting to speculate that rational combinatorial treatments targeting nonredundant mechanisms of immune resistance may enhance the efficacy of ICT in PDAC.

Here, immune and single-cell RNA sequencing (scRNA-seq) profiling of a murine PDAC model defined the TIME under various immune therapy perturbations. At baseline, the TIME was dominated by CXCR2-expressing myeloid-derived suppressor cells (MDSCs) and tumor-associated macrophages (TAMs), as well as $CD4^+$ regulatory T cells (T_{reg} cells) with high CTLA4 and OX40 expression and exhausted $CD8^+$ T cells with high PD-1, LAG3, 41BB and TIM3 expression. We hypothesized that de novo resistance of murine and human PDAC to anti-PD-1/anti-PD-L1 and/or anti-CTLA4 may relate to alternative immune checkpoints and/or cooperative immune-suppressive mechanisms across the fibrotic stroma, MDSCs and/or TAMs. To this end, single and combined ICT and targeted therapy, coupled with immune profiling, were used to identify an immunotherapy combination regimen capable of reinvigorating antitumor immunity in the TIME, leading to disease eradication in orthotopic tumors, as well as prolonged survival with durable remissions in autochthonous tumors. We validated the presence of these targets in human PDAC.

Results

Myeloid cells predominate in the iKRAS tumor microenvironment

The inducible oncogenic KRAS mouse model (p48-Cre; tetO_LSL-$Kras^{G12D}$; ROSA_rtTA; $p53^{L/+}$), designated iKRAS, recapitulates the hallmark features of human PDAC, including resistance to all standard therapies used to date[2,8]. For multiarm drug testing, several independently derived iKRAS cell lines were used to generate large cohorts with orthotopic PDAC tumors in syngeneic immunocompetent mice. Similar to autochthonous models, these orthotopic tumors grow rapidly to large volumes of ~1,000 mm^3, demonstrate avid fluorodeoxyglucose (FDG) uptake and can be detected using positron emission tomography/computed tomography, MRI and bioluminescence (Extended Data Fig. 1a,b). All mice succumb to PDAC after 3–8 weeks (Extended Data Fig. 1b). Mirroring human PDAC, the histological features of orthotopic and autochthonous murine iKRAS tumors include glandular tumor structures with moderately differentiated cells, significant desmoplasia with abundant collagen and high stromal expression of smooth muscle actin and vimentin, as well as local invasion into surrounding lymph nodes and organs such as the duodenum (Extended Data Fig. 1c–f).

To comprehensively audit the constellation of tumor-infiltrating immune cells, we performed time-of-flight mass cytometry (CyTOF), which confirmed a significant increase in $CD45^+$-infiltrating immune cells in established iKRAS tumors (4 weeks after initial detection on imaging; tumor volume = ~1,000 mm^3; Fig. 1a), consistent with human PDAC tumors (Extended Data Fig. 1f)[9,10]. A spanning-tree progression analysis of density-normalized events (SPADE)-derived tree[11] (Fig. 1b) revealed the complexity of the PDAC TIME with cancer cells ($EpCAM^+CD45^-$), non-immune tumor microenvironment (TME) cells ($EpCAM^-CD45^-$) and infiltrating immune subpopulations ($EpCAM^-CD45^+$). Autochthonous versus orthotopic iKRAS PDAC tumors possessed similar composition and relative proportions of various immune cells (Fig. 1c). Within the $CD45^+$-infiltrating immune cells, MDSCs ($CD45^+CD11b^+Gr1^+$) and TAMs ($CD45^+CD11b^+Gr1^-F4/80^+$) comprised a significant proportion of the immune population. The majority of MDSCs within the iKRAS PDAC TIME are neutrophilic/granulocytic in nature (Extended Data Fig. 1g). In coculture assays, these intratumoral $CD11b^+Gr1^+$ MDSCs suppressed anti-CD3 and anti-CD28 antibody-induced T cell proliferation and activation (interferon-γ (IFN-γ) production) (Fig. 1d,e), validating that $CD11b^+Gr1^+$ cells are indeed functional MDSCs[12]. Intratumoral MDSCs (characterized by S100A9 and arginase-1 expression[12]) and TAMs (characterized by F4/80 expression) were found directly adjacent to cancer cells in iKRAS tumors (Extended Data Fig. 1h,i), findings that mirror human tumor immune profiles. With respect to $CD3^+$ T cells, CyTOF revealed tumor-infiltrating $CD4^+$ and $CD8^+$ T cells (Fig. 1c). Using flow cytometry, the majority of intratumoral $CD4^+$ and $CD8^+$ T cells displayed an effector memory ($CD44^{hi}CD62L^{lo}$) phenotype (Fig. 1f), and among the $CD4^+$ T cells were a small proportion of $FoxP3^+$ T_{reg} cells (Extended Data Fig. 1j). Immunohistochemistry (IHC) analyses showed similar proportions and distributions of $CD8^+$ T cells and $S100A9^+$ MDSCs and their adjacency to cancer cells in autochthonous and orthotopic iKRAS tumors (Extended Data Fig. 1h). These murine findings aligned with those in human PDAC specimens (Extended Data Fig. 1k), which also included $CD8^+$ T cells with memory and cytotoxic phenotypes (Fig. 2a)[13].

Validating the fidelity of our murine models, IHC analysis of treatment-naive human PDAC tissues confirmed higher $CD11b^+$ myeloid cells, including $CD68^+$ macrophages and $CD15^+$ neutrophils/granulocytes (Extended Data Fig. 2a). Multiplex immunofluorescence showed $CD33^+CD11b^+CD66b^+$ neutrophils/granulocytes and $CD33^+CD14^+CD68^+$ TAMs in treatment-naive human PDAC tissues, consistent with previous studies of patients with PDAC and similar to iKRAS tumors (Fig. 2b)[9,10,14,15]. A 39-gene MDSC signature[13] and unsupervised clustering categorized 178 The Cancer Genome Atlas (TCGA) primary PDAC tumors into MDSC-high ($n = 114$), MDSC-medium ($n = 54$) and MDSC-low ($n = 10$) subgroups, revealing that 94% tumors had either MDSC-high or -medium signatures (Extended Data Fig. 2b). CIBERSORTx analysis of immune cell subsets in PDAC TCGA and ICGC-AU cohorts to enumerate the fractions of immune cell subsets[16] revealed macrophages/monocytes as the predominant immune cell types (Fig. 2c). While CIBERSORTx cannot deconvolute MDSCs from macrophages and other myeloid cells, this analysis showed that the predominant macrophage/monocyte population displayed an immunosuppressive

Fig. 1 | Prominent infiltration of myeloid immunosuppressive cells in iKRAS tumors. a, Quantification of tumor-infiltrating $CD45^+$ cells in syngeneic iKRAS tumors, as assessed by CyTOF at 4 weeks after initial tumor detection ($n = 10$ samples per group). Statistical significance was determined by two-sided Student's *t*-test. **b**, SPADE tree derived from CyTOF analysis of a whole-tumor cell population from syngeneic iKRAS PDAC tumors ($n = 10$ tumors). Live single cells were used to construct the tree. Cell populations were identified as PDAC cells ($EpCAM^+CD45^-$), nonimmune TME cells ($EpCAM^-CD45^-$), CD4 or CD8 T cells ($CD45^+CD3^+TCR\beta^+$), B cells ($CD45^+B220^+CD19^+$), natural killer (NK) cells ($CD45^+NK1.1^+$), dendritic cells ($CD45^+CD11c^+$), MDSCs ($CD45^+CD11b^+Gr1^+$) and macrophages (Mø; $CD45^+CD11b^+Gr1^-F4/80^+$). **c**, CyTOF analysis of tumors from syngeneic and autochthonous iKRAS PDAC tumors with an equivalent tumor volume (~1,000 mm^3) ($n = 10$ samples per group). **d**, Left, representative CFSE flow cytometry histograms showing the effect on in vitro T cell proliferation by MDSCs isolated from iKRAS tumors. Right, summarized results. Unstimulated T cells were used as a negative control. The position of the CFSE peaks can be used to denote the T cell division times. High and low proliferation were defined as T cell divisions of ≥2 and ≤1, respectively ($n = 3$ biological replicates). **e**, Effect on IFN-γ secretion from $CD8^+$ T cells by MDSCs isolated from iKRAS tumors, as measured by enzyme-linked immunosorbent assay ($n = 3$ biological replicates). Statistical significance was determined by two-sided Student's *t*-test. **f**, Quantification of tumor-infiltrating $CD4^+$ and $CD8^+$ T cells in iKRAS tumors ($n = 3$ biological replicates), as assessed by flow cytometry and analyzed by FlowJo. Cell populations were identified as naive ($CD44^{low}CD62L^{high}$), central memory ($CD44^{high}CD62L^{high}$) or effector memory ($CD44^{high}CD62L^{low}$). The data in **a**,**e**,**f** are presented as means ± s.e.m.

https://doi.org/10.1038/s43018-022-00500-z

M2-like macrophage signature (Extended Data Fig. 2c). Correspondingly, IHC analysis of human PDAC tumors showed increased CD163$^+$ M2 macrophages (Extended Data Fig. 2d).

Humans and mice possess two TAM subtypes (Spp1$^+$ and C1q$^+$) with distinct origins and functions[17]. Using TAM subtype gene signatures[17], higher Spp1$^+$ TAM frequency, but not C1q$^+$, correlated

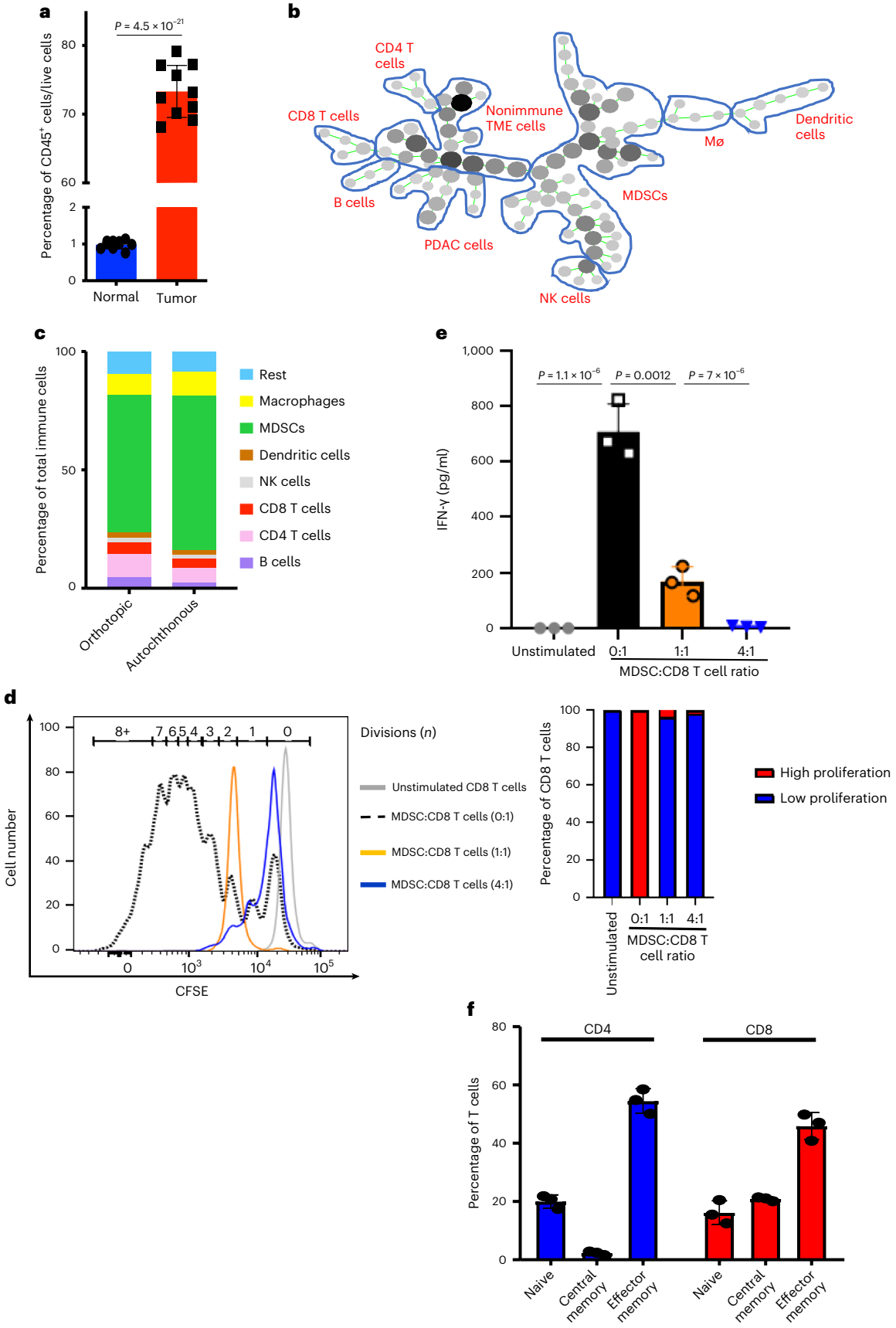

https://doi.org/10.1038/s43018-022-00500-z

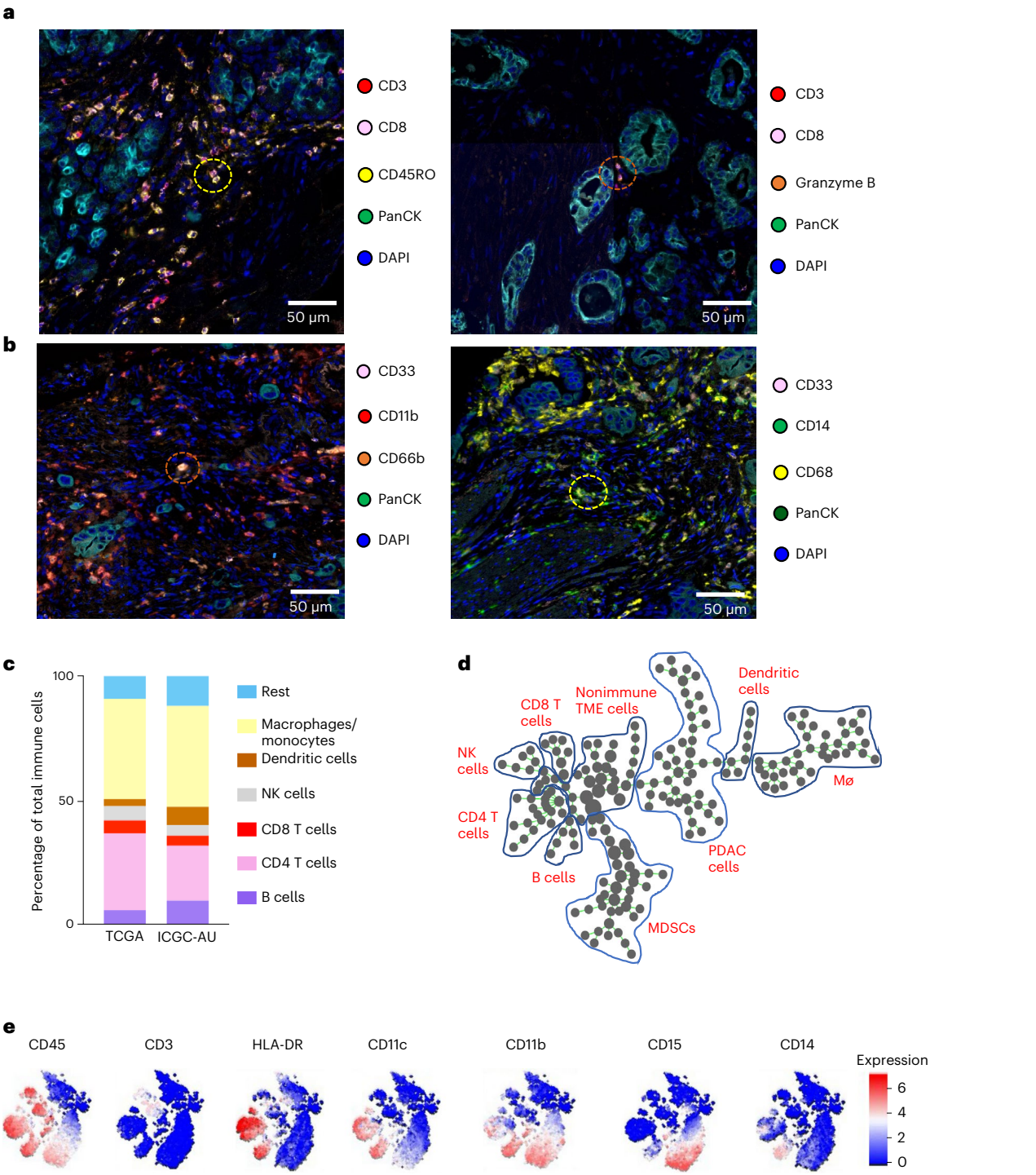

Fig. 2 | Prominent infiltration of myeloid immunosuppressive cells in human PDAC tumors. a,**b**, Representative multiplex immunofluorescence images of human PDAC tissues on formalin-fixed, paraffin-embedded slides stained with CD3, CD8, panCK, 4′,6-diamidino-2-phenylindole (DAPI) and either CD45RO or granzyme B (**a**) or CD33, panCK, DAPI and either CD11b and CD66b or CD14 and CD68 (**b**). Each experiment was replicated twice with similar results. Dashed circle represents cell type with indicated expression profile. **c**, CIBERSORTx quantification of immune cell subsets in human PDAC samples: TCGA ($n = 178$ patients) and ICGC-AU ($n = 92$ patients). **d**, SPADE tree derived from CyTOF analysis of a whole-tumor cell population from human PDAC samples ($n = 5$ patients). Live single cells were used to construct the tree. See Supplementary Table 1 for clinicopathologic and demographic information about patients and Supplementary Table 2 for antibodies. Cell populations were identified as PDAC cells ($EpCAM^+CD45^-$), nonimmune TME cells ($EpCAM^-CD45^-$), CD4 T cells ($CD45^+CD3^+CD4^+$), CD8 T cells ($CD45^+CD3^+CD8^+$), B cells ($CD45^+CD19^+$), NK cells ($CD45^+CD161^+CD56^+$), dendritic cells ($CD45^+CD33^+HLA\text{-}DR^+CD14^-CD15^-CD16^-CD11c^+$), MDSCs ($CD45^+CD33^+HLA\text{-}DR^-CD11b^+CD14^-CD15^+$ (neutrophilic/granulocytic) or $CD45^+CD33^+HLA\text{-}DR^-CD11b^+CD14^+CD15^-$ (monocytic)) and macrophages ($CD45^+CD33^+HLA\text{-}DR^+CD14^+CD15^-CD16^-CD11c^+$). **e**, CyTOF analysis of human PDAC tumors ($n = 5$ patients). See Supplementary Table 1 for clinicopathologic and demographic information about patients and Supplementary Table 2 for antibodies. Red indicates a high level of expression of the indicated marker. Blue indicates no marker expression.

https://doi.org/10.1038/s43018-022-00500-z

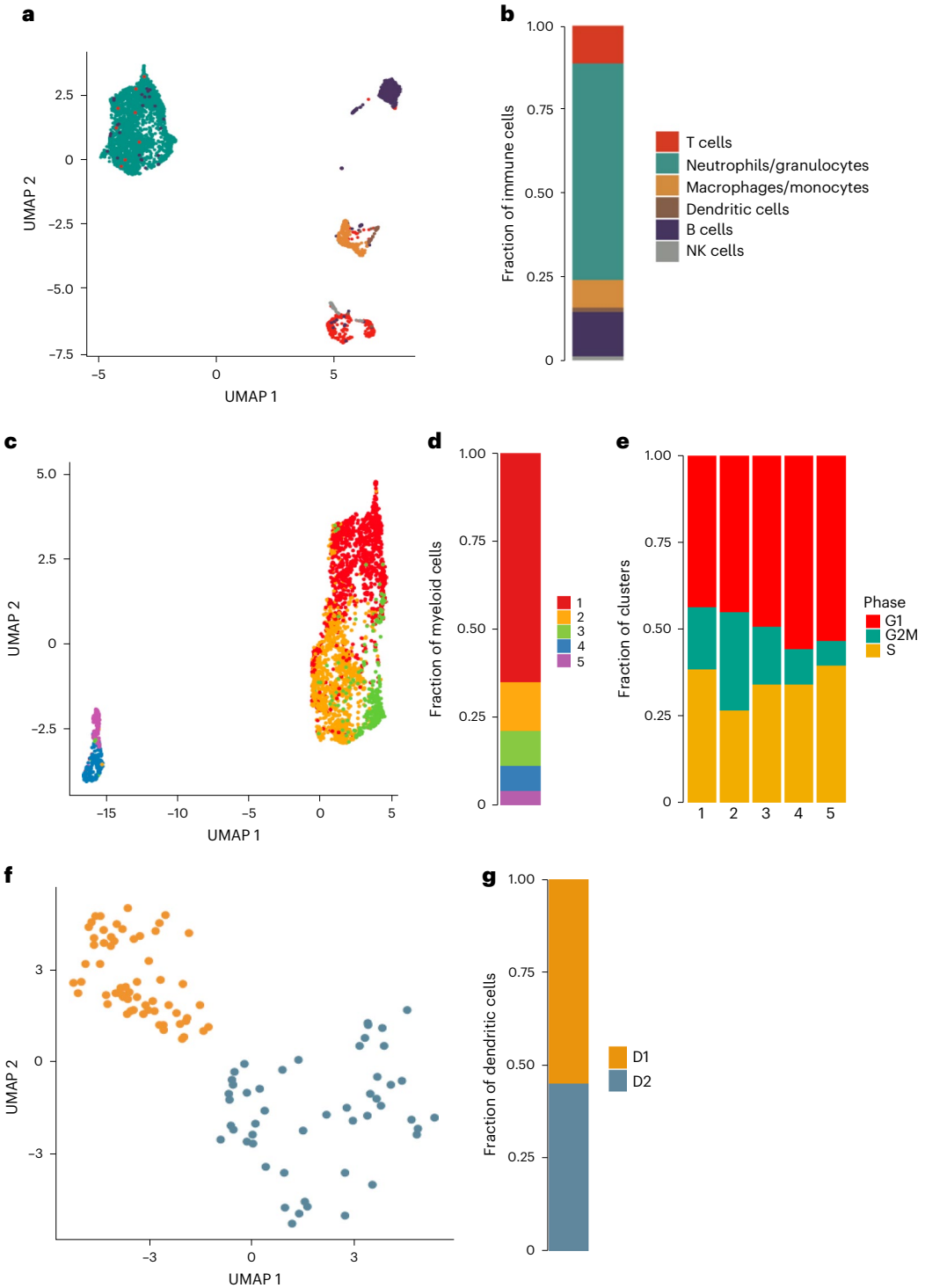

Fig. 3 | Heterogeneity of myeloid cells in three iKRAS PDAC tumors identified by single-cell gene expression profiling. a, UMAP projection of immune cell clusters. **b**, Proportion of immune cell subtypes. **c**, UMAP projection of myeloid cell clusters. **d**, Proportion of myeloid cell subtypes. **e**, Cell cycle scoring for five myeloid cell clusters. **f**, UMAP projection of dendritic cell clusters. **g**, Proportion of dendritic cell subtypes.

with significantly lower overall survival in the PDAC TCGA cohort (Extended Data Fig. 2e). Given that neoadjuvant chemotherapy or radiation can reshape the PDAC TIME[15], a validated CyTOF panel assessed myeloid cell representation in fresh PDAC specimens from patients who completed neoadjuvant chemotherapy and/or radiation ($n = 5$) (Supplementary Tables 1 and 2)[18]. MDSCs and macrophages were confirmed to be the major immune cell subpopulations by SPADE analysis (Fig. 2d) and, similar to iKRAS tumors, the majority of MDSCs within the human PDAC TIME were neutrophilic/granulocytic (Fig. 2e). In summary, two major populations of immunosuppressive myeloid cells—neutrophils/granulocytes and macrophages—are present in treatment-naive and chemotherapy- or radiation-treated human PDAC specimens. In addition, we detected intratumoral memory and cytotoxic $CD8^+$ T cells, although these T cells become progressively exhausted or dysfunctional, as described previously[10,15,19–21].

https://doi.org/10.1038/s43018-022-00500-z

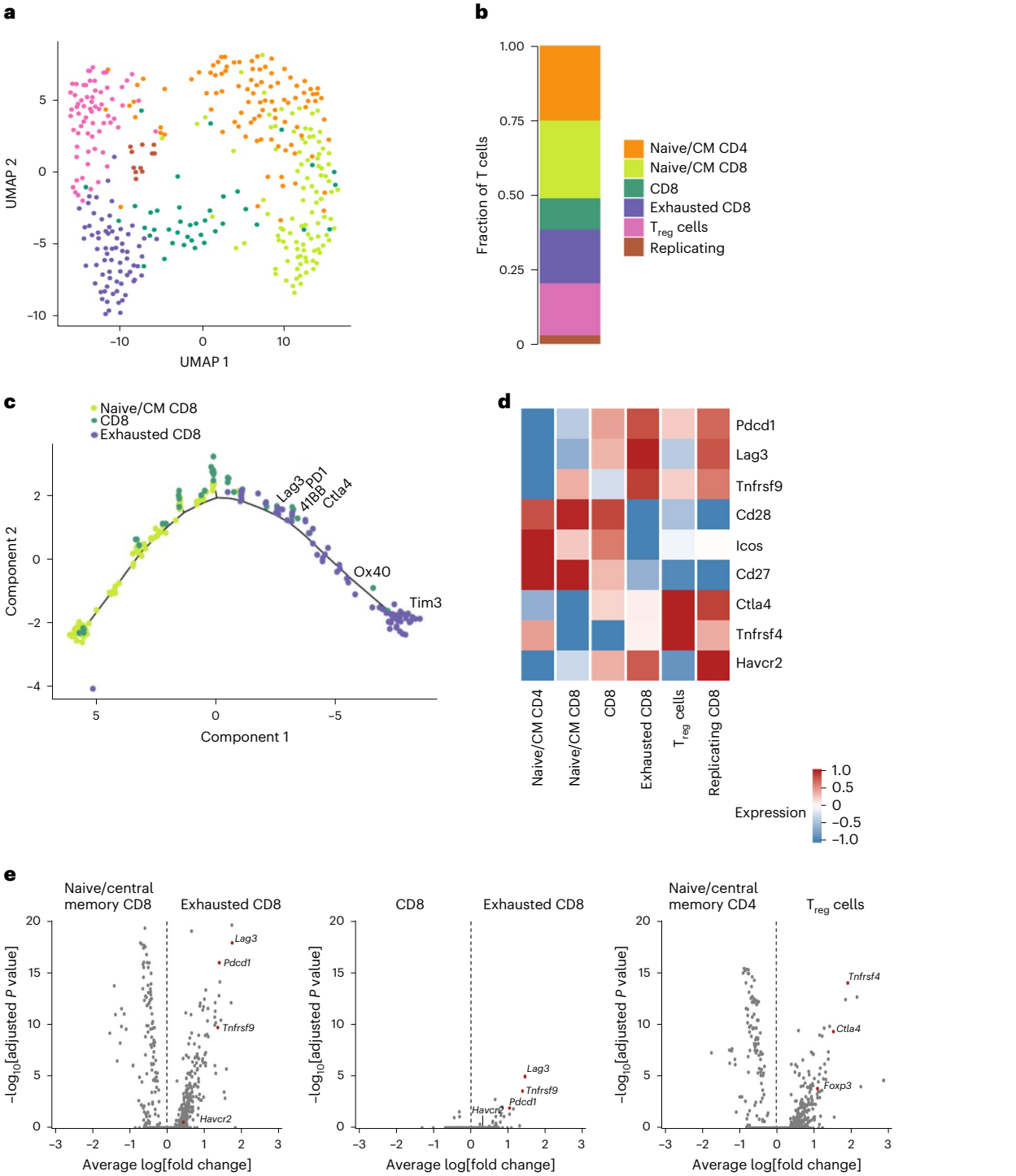

Fig. 4 | Dysfunctional phenotype of T cells in three iKRAS PDAC tumors identified by single-cell gene expression profiling. a, UMAP projection of T cell clusters. **b**, Proportion of T cell subtypes. **c**, Ordering of CD8$^+$ T cells along pseudotime in a two-dimensional state space defined by Monocle2. Each point corresponds to a single cell and each color represents a CD8$^+$ T cell cluster. **d**, Heatmap of immune checkpoint expression on various clusters of CD4$^+$ and CD8$^+$ T cells. **e**, Volcano plot showing differentially expressed genes between naive or central memory CD8$^+$ T cells and exhausted CD8$^+$ T cells (left), CD8$^+$ T cells and exhausted CD8$^+$ T cells (middle) and naive or central memory CD4$^+$ T cells and T$_{reg}$ cells (right).

The dysfunctional phenotype of T cells in iKRAS tumors

To delineate the immune composition and heterogeneity of iKRAS tumors, scRNA-seq was performed on live CD45$^+$ immune cells sorted from tumors harvested at 4 weeks after initial detection on imaging (tumor volume = ~1,000 mm^3). A total of 4,080 sorted individual immune cells from three iKRAS tumors were sequenced to an average depth of 50,000 reads per cell (Extended Data Fig. 3a). Dimensional reduction analysis (uniform manifold approximation and projection (UMAP)) and clustering applied to the expression data revealed that live CD45$^+$ immune cells clustered into several subgroups with similar fractions (Fig. 3a,b) to those identified by CyTOF analysis of orthotopic and autochthonous iKRAS tumors (Fig. 1c). Specifically, signature genes and known functional markers identified neutrophils/granulocytes (*S100A8*, *S100A9* and *Gos2* expression), macrophages/monocytes

https://doi.org/10.1038/s43018-022-00500-z

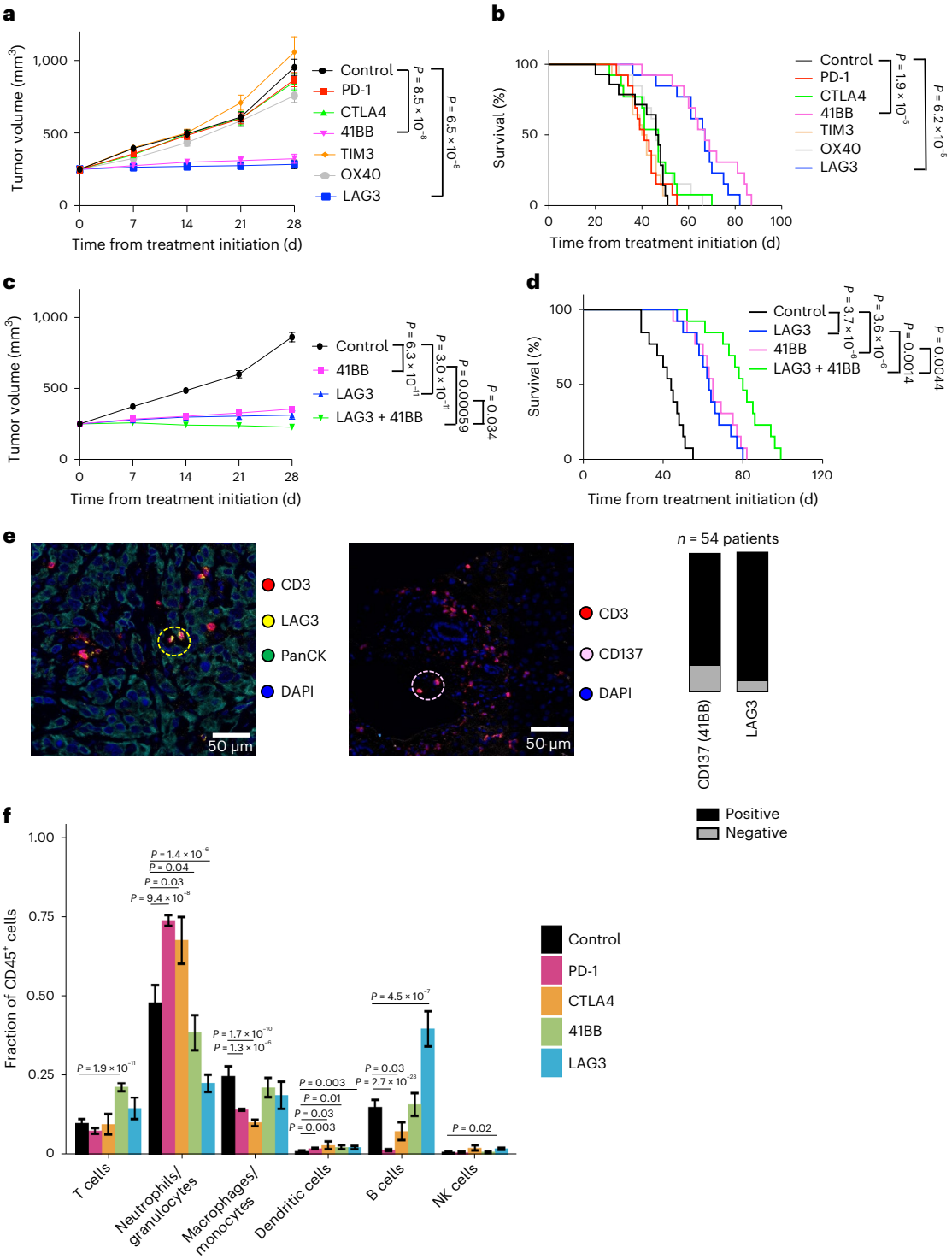

Fig. 5 | Efficacy of ICT and treatment effects on the immune microenvironment. a, Tumor volume after 4 weeks of treatment with control, anti-PD-1, anti-CTLA4, anti-41BB, anti-TIM3, anti-OX40 or anti-LAG3 antibody in mice bearing established (tumor volume = ~250 mm^3 before treatment initiation) orthotopic iKRAS tumors ($n = 13$ or 14 mice per group). **b**, Overall survival of mice bearing established orthotopic iKRAS tumors (tumor volume = ~250 mm^3 before treatment initiation) treated with control, anti-PD-1, anti-CTLA4, anti-41BB, anti-TIM3, anti-OX40 or anti-LAG3 antibody ($n = 13$ or 14 mice per group). **c**, Tumor volume after 4 weeks of treatment with control, anti-41BB, anti-LAG3 or anti-41BB + anti-LAG3 antibodies in mice bearing established orthotopic iKRAS tumors (tumor volume = ~250 mm^3 before treatment initiation) ($n = 13$ mice per group). **d**, Overall survival of mice bearing established orthotopic iKRAS tumors (tumor volume = ~250 mm^3 before treatment initiation) treated with control, anti-41BB, anti-LAG3 or anti-41BB + anti-LAG3 antibodies ($n = 13$ mice per group). **e**, Left and middle, representative spectral composite images of immunofluorescence staining for the indicated proteins in human PDAC samples. Each experiment was replicated twice with similar results. Right, quantification of the proportion of human PDAC samples with positive and negative staining for the indicated proteins ($n = 54$ patients). Dashed circle represents cell type with indicated expression profile. **f**, Quantification of the change in the proportion of immune cell subtypes in single-cell sequencing analysis of established iKRAS tumors (tumor volume = ~250 mm^3 before treatment initiation) after treatment with anti-PD-1, anti-CTLA4, anti-41BB or anti-LAG3 antibody for 4 weeks ($n = 3$ tumors per group). Statistical significance was determined by two-sided Student's *t*-test (**a**,**c**), Kaplan–Meier survival curves and log-rank test (**b**,**d**) or mixed-effect model (**f**). The data in **a**,**c**,**f** are presented as means ± s.e.m.

(*Mafb*, *C1qa*, *C1qc*, *Apoe*, *Lgmn* and *Spp1* expression), B cells (*Cd79* expression), T cells (*Cd3* expression), natural killer cells (*Klr* and *Ncr1* expression) and dendritic cells (*Fscn1* and *Ccl22* expression) (Extended Data Fig. 3b,c). Neutrophils/granulocytes and macrophages/monocytes in the myeloid compartment were the predominant immune cells in the iKRAS TIME, as demonstrated by both CyTOF (Fig. 1c) and scRNA-seq (Fig. 3a,b and Extended Data Fig. 3b,c), consistent with human PDAC[9,14,15] (Fig. 2d).

Myeloid cells, including neutrophils/granulocytes and macrophages/monocytes, exhibit subtle differences in their cell states, existing along a continuum rather than under discrete phenotypic states[12,17,22–24]. There is a high degree of plasticity within the myeloid population in PDAC, as well as significant phenotypic heterogeneity between mouse and human myeloid cells[9,10,14,15,25,26]. To evaluate the intrinsic myeloid cell heterogeneity in iKRAS tumors, we applied clustering and identified five myeloid cell clusters (Myeloid_c1–5) with differential expression of signature genes and known functional markers (Fig. 3c,d, Extended Data Fig. 3d,e and Supplementary Table 3). Both myeloid_c2 and myeloid_c3 clusters showed *Cxcr2* and *Ly6g* expression consistent with previous studies describing CXCR2 expression on neutrophils/granulocytes or neutrophilic/granulocytic MDSCs[27,28]. All myeloid cell clusters exhibited low replicative potential based on cell cycle scoring genes (Fig. 3e). Classical dendritic cells, which are critical for antigen priming, T cell activation and ICT responsiveness[2,4], were present in iKRAS tumors (Fig. 3f,g, Extended Data Fig. 3f and Supplementary Table 3).

To further characterize intratumoral T cell populations, we performed unsupervised clustering and identified six clusters, including two clusters of $CD4^+$ (CD4_c1 and CD4_c2) and four clusters of $CD8^+$ T cells (CD8_c1, CD8_c2, CD8_c3 and CD8_c4) (Fig. 4a,b), which clearly aligned with subsets in human PDAC[10,11,28] and other tumors[29]. The two clusters of $CD4^+$ T cells included naive or central memory $CD4^+$ T cells (CD4_c1; *Ccr7*, *Sell* (encoding CD62L) and *Lef1* expression) and T_{reg} cells (CD4_c2; *Foxp3* expression, as well as *Ctla4* and *Tnfrsf4* (OX40) expression) (Extended Data Fig. 4a,b). $CD8^+$ T cell clusters included naive or central memory $CD8^+$ T cells (CD8_c1; *Ccr7*, *Sell* (encoding CD62L) and *Lef1* expression), two separate clusters (CD8_c2 and CD8_c3) with expression of cytotoxic genes (*Nkg7* and *Gzmb*)—although one of these clusters displayed higher expression of T cell exhaustion markers including *Pdcd1*, *Lag3* and *Havcr2*, consistent with exhausted $CD8^+$ T cells (CD8_c3)—and a small cluster of highly replicating $CD8^+$ T cells (CD8_c4; high *Ki-67* and *Stmn1* expression, as well as expression of the antiapoptotic gene *Birc5* (refs. 30, 31)) (Extended Data Fig. 4a,b). We validated the high replicative potential of the CD8_c4 cluster using cell cycle scoring genes (Extended Data Fig. 4c). Notably, a subset of T cells in the PDAC TIME were naive or central memory cells based on scRNA-seq (Fig. 4a,b and Extended Data Fig. 4a,b), consistent with our previous findings using flow cytometry (Fig. 1f). Both clusters of naive or central memory T cells (CD4_c1 and CD8_c1) expressed *TCF7* (encoding the transcription factor T cell factor 1), which has been associated with a progenitor or stem-like state, ICT response and improved outcomes[32,33] (Extended Data Fig. 4b).

We further interrogated the developmental trajectory of $CD8^+$ T cells within the PDAC TME using Monocle2 (ref. 34). Clusters of $CD8^+$ T cells formed a linear structure, which when rooted with naive or central memory $CD8^+$ T cells was followed by nonexhausted cytotoxic $CD8^+$ T cells and ended with exhausted $CD8^+$ T cells (Fig. 4c). Thus, exhausted T cells were highly enriched at the late period of pseudotime—a pattern consistent with the $CD8^+$ T cell state transition from naive or central memory to activated or nonexhausted to exhausted. Exhausted T cells expressed high levels of granzyme B (*GzmB*) with low levels of granzyme K (*GzmK*) (Extended Data Fig. 4d). The expression of genes encoding activating (*Tnfrsf9* and *Tnfrsf4*) and inhibitory (*Pdcd1*, *Lag3*, *Ctla4* and *Havcr2*) immune checkpoints was noted on the exhausted $CD8^+$ T cell cluster but not in the naive/central memory or intermediate nonexhausted/activated $CD8^+$ T cell states (Fig. 4c–e and Extended Data Fig. 4d), raising the possibility that these molecules may mediate the exhausted state of $CD8^+$ T cells in the PDAC TIME. We found preferential enrichment of $CD4^+$ T_{reg} cells with high *Ctla4* and *Tnfrsf4* expression, as well as exhausted $CD8^+$ T cells with high *Pdcd1*, *Lag3*, *Tnfrsf9* and *Havcr2* expression among the differentiated T cell population in PDAC (Fig. 4d,e). Flow cytometry validated the expression of these immune checkpoint molecules on $CD4^+$ and $CD8^+$ T cells (Extended Data Fig. 4e). Since exhausted T cells and T_{reg} cells are targets for cancer immunotherapies[2,4], we focused our analyses on the role of hitherto uncharacterized immune checkpoints, where the consequences of targeting each checkpoint in PDAC are not known.

Efficacy of agonist 41BB and antagonist LAG3 ICTs in iKRAS tumors

The presence of intratumoral $CD8^+$ T cells in iKRAS models (Fig. 1c and Extended Data Fig. 1h), together with improved overall survival associated with increased $CD8^+$ T cell infiltration and their proximity to cancer cells in human PDAC[21,35–37], and the lack of efficacy of PD-1/CTLA4 in clinical trials[4–7], prompted us to consider the presence of a poised immune microenvironment that can be activated by targeting alternate immune checkpoints. To test this hypothesis, immunocompetent C57BL/6 mice with orthotopic iKRAS tumors were treated with agonist and antagonist ICT antibodies targeting the aforementioned checkpoints expressed on differentiated T cells in iKRAS tumors (Extended Data Fig. 5a). Mice with MRI-documented PDAC of equivalent size were treated with a single high dose of gemcitabine (100 mg/kg)[38] and subsequently randomized to receive single or combination ICT treatments for 4 weeks before endpoint analysis (Extended Data Fig. 5a). Gemcitabine, a standard chemotherapy treatment, was administered to provoke tumor cell death and release neoantigens, as well as decrease MDSC and T_{reg} cell accumulation and activity in murine PDAC tumors, as reported previously[3,39,40].

Consistent with human clinical trials, antagonist PD-1 and CTLA4 antibodies had no effect on tumor growth or overall survival (Fig. 5a,b)[5–7]. Although a prevailing view holds that this poor response relates to poor infiltration of effector T cells, the above immune profiles clearly show tumor-infiltrating $CD4^+$ and $CD8^+$ T cells with high *Ctla4* and *Pdcd1* expression. In exploring alternative immune checkpoints,

Fig. 6 | Effects of ICT treatment on the immune microenvironment. **a**, Fraction of top clonotypes in each T cell cluster among control and anti-41BB antibody-treated mice ($n = 3$ mice per group). **b**, Relative expression levels of *Gzmk* and *Gzmb* among T cells in control and anti-41BB antibody-treated mice ($n = 3$ mice per group). Statistical significance was determined by two-sided unpaired Wilcox test (*$P < 0.05$). **c**, Relative expression of gene signatures of T cell inhibition[43], terminal differentiation[24], progenitor exhaustion[32] and terminal exhaustion[27] in T cells from clusters T_c1 and T_c3. ($n = 1{,}762$ cells (T_c1) and 1,809 cells (T_c3)). Statistical significance was determined by two-sided unpaired Wilcox test (*$P < 0.05$). **d**, Fraction of overlapping TCR CDR3 sequences between mice after 4 weeks of treatment with control, anti-PD-1, anti-CTLA4, anti-41BB or anti-LAG3 antibody in mice bearing established orthotopic iKRAS tumors (tumor volume = ~250 mm^3 before treatment initiation) ($n = 3$ mice per group). **e**, Fraction of $CD3^+CD4^-CD8^-NK1.1^-$ T cells among $CD3^+$ T cells after 4 weeks of treatment with control, anti-PD-1, anti-CTLA4, anti-41BB or anti-LAG3 antibody in mice bearing established orthotopic iKRAS tumors (tumor volume = ~250 mm^3 before treatment initiation) ($n = 3$ mice per group). Statistical significance was determined by mixed-effect model. The data are presented as means ± s.e.m. **f**, Relative expression of *Il17a* among subtypes of $CD3^+$ T cells. **g**, Violin plots showing the expression of β2m, H2-Aa, Cd74 and H2-Ab1 among myeloid cells from control, anti-PD-1, anti-CTLA4, anti-41BB and anti-LAG3 antibody-treated tumors ($n = 3$ tumors per group). Statistical significance was determined by two-sided unpaired Wilcox test (*$P < 0.05$).

https://doi.org/10.1038/s43018-022-00500-z

we detected increased *Lag3*, *Tnfrsf9* (41BB) and *Havcr2* (TIM3) expression in response to anti-PD-1 or anti-CTLA4 monotherapy relative to control antibody treatment (Extended Data Fig. 5b). Conversely, we noted decreased *Tnfrsf4* (OX40) expression in response to anti-PD-1 and anti-CTLA4 monotherapy. Given these immune checkpoint profiles, tumor-bearing mice were treated with agonist (41BB and OX40) or antagonist (LAG3 and TIM3) antibodies as monotherapy. Strikingly, impaired PDAC progression and increased overall survival were observed with agonist 41BB and antagonist LAG3 antibodies (Fig. 5a,b). Combined agonist 41BB and antagonist LAG3 antibody treatment, which was well tolerated during the 4-week treatment period, produced significantly increased survival relative to either monotherapy (Fig. 5c,d). However, all dual ICT-treated mice eventually succumbed. These unexpected murine findings prompted analysis of

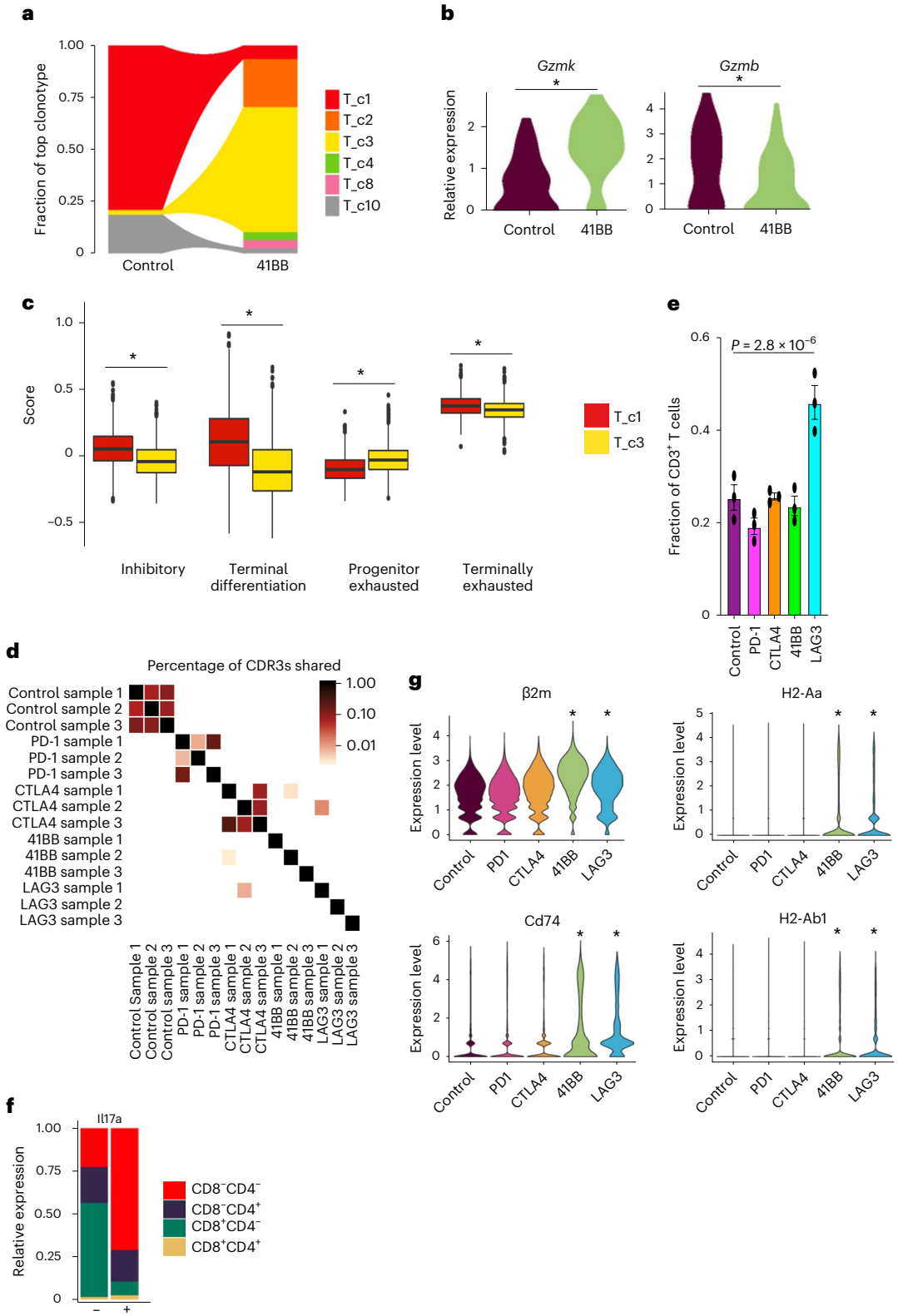

41BB and LAG3 expression in treatment-naive human PDAC specimens (n = 54 patients) (Fig. 5e). Using multiplex immunofluorescence, 81% of specimens from patients with PDAC exhibited 41BB$^+$ T cells, while 93% exhibited LAG3$^+$ T cells. Notably, both 41BB and LAG3 were elevated on tumor-infiltrating T cells compared with circulating T cells in human patients with PDAC[21].

Furthermore, analysis of 41BB and LAG3 expression via scRNA-seq of 40 treatment-naive human patients with PDAC from two datasets validated the expression of 41BB and LAG3 on T cells in human PDAC (Extended Data Fig. 5c)[10,26]. Since coexpression of multiple coinhibitory receptors results in a dysfunctional or exhausted phenotype of T cells[41], we examined the coinhibitory receptor expression of 41BB and LAG3 on tumor-infiltrating CD8$^+$ T cells in iKRAS tumors. We found that <0.5% of CD8$^+$ T cells examined coexpressed 41BB and LAG3, suggesting that 41BB and LAG3 axes may represent nonredundant mechanisms of T cell exhaustion, which further supports strategies that cotarget these checkpoints. Thus, activation of T cell activity and antitumor activity with agonist 41BB and/or antagonist LAG3 antibodies in iKRAS PDAC tumors, coupled with comparable target expression in human PDAC, portends translational relevance.

To evaluate dynamic changes in the TIME with the various ICT agents, scRNA-seq was used to examine various immune cell subpopulations and their transcriptional changes in iKRAS tumors following a 4-week treatment period with effective (agonist 41BB and antagonist LAG3) and ineffective (antagonist PD-1 and CTLA4) agents compared with a control (n = 3 per treatment group) (Extended Data Fig. 5a). Single-cell analysis of sorted CD45$^+$ immune cells yielded data on a total of 72,440 cells with an average depth of 50,000 reads per cell (Extended Data Fig. 5d). To define the subpopulation structure, we computationally pooled data from the various treatment groups and subsequently identified transcriptional clusters consisting of individual cell types (Extended Data Figs. 5e–f and 6a). Dimensional reduction analysis (UMAP) revealed that immune cells clustered into similar subtypes of immune cells as untreated tumors (Fig. 3a,b and Extended Data Figs. 3b,c, 5e–f and 6a). Compared with untreated tumors (Figs. 3a–d and 4a,b and Extended Data Figs. 3b–e and 4a,b), several T cell (Extended Data Fig. 6b,c), neutrophil/granulocyte (Extended Data Figs. 6d and 7a) and macrophage/monocyte (Extended Data Fig. 7b,c) clusters were identified, which were unique to treated tumors. A total of five CD8$^+$ and four CD4$^+$ T cell clusters were identified, including naive or central memory CD4$^+$ (T_c5) and CD8$^+$ cells (T_c4), exhausted CD8$^+$ (T_c1), effector CD4$^+$ (T_c2 and T_c6) and CD8$^+$ cells (T_c3 and T_c8), T_{reg} cells (T_c7), T helper 17 cells (T_c9) and replicating CD8$^+$ cells (T_c10) (Extended Data Fig. 6b,c). Myeloid cells were classified as either neutrophils/granulocytes (characterized by the expression of *S100A8*, *S100A9* and *Gos2*, which are also highly expressed in neutrophils/granulocytes in human PDAC[9,26]) or macrophages/monocytes (characterized by the expression of *Apoe* (associated with noninflammatory, immunosuppressive macrophages), *Spp1*, *Lyz2* (expressed by classical monocytes[10]), *C1qa/c* (associated with tissue-resident macrophages[10]) and *Arg1* (suggestive of immunosuppressive potential[14])), consistent with clustering in untreated iKRAS tumors (Fig. 3c,d and Extended Data Figs. 3d,e, 5e,f and 6a). Further interrogation of myeloid cell heterogeneity revealed a continuum of states, which resolved into five neutrophil/granulocyte clusters (N_c1–5; Extended Data Figs. 6d and 7a and Supplementary Table 3) and five macrophage/monocyte clusters (M_c1–5; Extended Data Fig. 7b,c and Supplementary Table 3), consistent with recently described subsets in other human and murine tumors[17,23]. N_c3 was characterized by *Cxcr2* expression, which is implicated in MDSC and neutrophil migration into PDAC[27,28].

Treatment with the ineffective antagonists PD-1 and CTLA4 did not significantly impact the T cell infiltrates, whereas agonist 41BB antibody treatment resulted in T cell expansion, predominated by nonexhausted cytotoxic CD8$^+$ T cells expressing high *Ccl5*, high *GzmK* and low *GzmB* (Fig. 5f and Extended Data Figs. 7d and 8a). 41BB-treated T cells were enriched in cluster T_c3, compared with control-treated T cells, which were enriched in cluster T_c1 (Fig. 6a). 41BB treatment elicited a shift in expression from *GzmB*-high to *GzmK*-high T cells (Fig. 6b). *GzmK*-expressing predysfunctional effector memory T cells have a less exhausted phenotype compared with *GzmB*-expressing dysfunctional exhausted T cells[29,33,42]. Comparing gene signatures of CD8$^+$ T cell inhibition[43], terminal differentiation[24], progenitor exhaustion[32] and terminal exhaustion[33] in T cells from clusters T_c1 and T_c3 (Fig. 6c), we found that the expression of gene signatures of inhibition, terminal differentiation and terminal exhaustion was significantly enriched in *GzmB*-expressing cells (T_c1) compared with *GzmK*-expressing cells (T_c3). Meanwhile, *GzmK*-expressing cells (T_c3) were significantly enriched in the expression of the progenitor-exhausted gene signature (associated with ICT response[32]) compared with *GzmB*-expressing cells (T_c1). Pathway analysis revealed upregulation of intracellular signaling, cytokine production, proliferation and cytolytic activity in T cells from 41BB-treated iKRAS tumors compared with control (Extended Data Fig. 8b), consistent with previous studies[44–46].

T cell clonality is lower in PDAC compared with colorectal cancer and melanoma, consistent with the relative paucity of coding mutations[47–49]. While T cells in human PDAC display minimal clonal expansion, higher clonality scores trend toward increased T cell receptor (TCR) signaling and effector phenotype[21], and a higher number of expanded T cell clones correlates with improved overall survival in patients with PDAC receiving ICT[50]. Therefore, in iKRAS tumors, the TCR repertoire was evaluated using single-cell TCR sequencing matched with transcriptome data to assess changes in phenotype, clonality and TCR sequences after ICT treatment. 41BB treatment resulted in CD8$^+$ cell clonotype expansion, comprised mainly of nonexhausted cytotoxic T cells (cluster T_c3), while cells from the control group were enriched in clusters T_c4 and T_c5 (Extended Data Fig. 8a,c). Cells from the most expanded TCRs were almost exclusively in cluster T_c3. None of the other ICT agents tested (PD-1, CTLA4 and LAG3) impacted the clonality of T cells. Next, we evaluated TCR diversity, which decreases with progressive exhaustion of T cells[43] and tracks with poor outcomes[51]. TCR diversification is associated with improved therapeutic benefit from ICT treatment[50,52]. Upon evaluation of the overlap in TCR CDR3 sequences from T cells, anti-PD-1- and anti-CTLA4-treated mice harbored significant overlap among TCRs between mice within their

Fig. 7 | Efficacy of targeted therapy directed against Cxcr1/2 and treatment effects on the immune microenvironment. a, Overall survival of mice bearing established orthotopic iKRAS tumors (tumor volume = ~250 mm^3 before treatment initiation) treated with control or anti-Gr1 neutralizing antibody for 4 weeks (n = 10 mice per group). **b**, Overall survival of mice bearing established orthotopic iKRAS tumors (tumor volume = ~250 mm^3 before treatment initiation) treated with control or SX-682 for 4 weeks (n = 10 mice per group). **c**, Quantification of total CD45$^+$ immune cells, CD4$^+$ and CD8$^+$ T cells and granulocytic and monocytic MDSCs (Gr-MDSC and MO-MDSC, respectively) in established iKRAS tumors (tumor volume = ~250 mm^3 before treatment initiation) treated with control, SX-682 or a combination therapy (anti-LAG3 + anti-41BB + SX-682) for 4 weeks, as assessed by flow cytometry and analyzed by FlowJo (n = 3 biological replicates). **d**, Relative expression of *Ifng* and *Tnf* on T cells in scRNA-seq analysis of iKRAS tumors following treatment with control, SX-682 or a combination therapy (anti-LAG3 + anti-41BB + SX-682) (n = 3 tumors per group). *P < 0.05. **e**, Multiple testing-corrected 95% binomial confidence intervals on the probability of a cell in each treatment group containing a TCR CD3R sequence overlapping that of another cluster. *P < 0.05. **f**, Overall survival of mice bearing established orthotopic iKRAS tumors (tumor volume = ~250 mm^3 before treatment initiation) treated with control, SX-682 or SX-682 with CD8 T cell depleting monoclonal antibody (CD8 mAb) (n = 10 mice per group). Statistical significance was determined by Kaplan–Meier survival curves and log-rank test (**a**,**b**,**f**), two-sided Student's t-test (**c**) or two-sided unpaired Wilcox test (**d**). The data in **c**,**d** are presented as means ± s.e.m.

https://doi.org/10.1038/s43018-022-00500-z

treatment group, similar to the control group (Fig. 6d and Extended Data Fig. 8d). In striking contrast, agonist 41BB and antagonist LAG3 antibody treatments elicited complete loss of TCR overlap, consistent with TCR diversification.

While LAG3 treatment did not increase T cell infiltration into iKRAS tumors (Fig. 5f and Extended Data Fig. 7d), treatment doubled the fraction of $CD3^+CD4^-CD8^-NK1.1^-$ T cells, which are known targets of ICT and have antitumor effects in PDAC and other tumor types[53–55] (Fig. 6e).

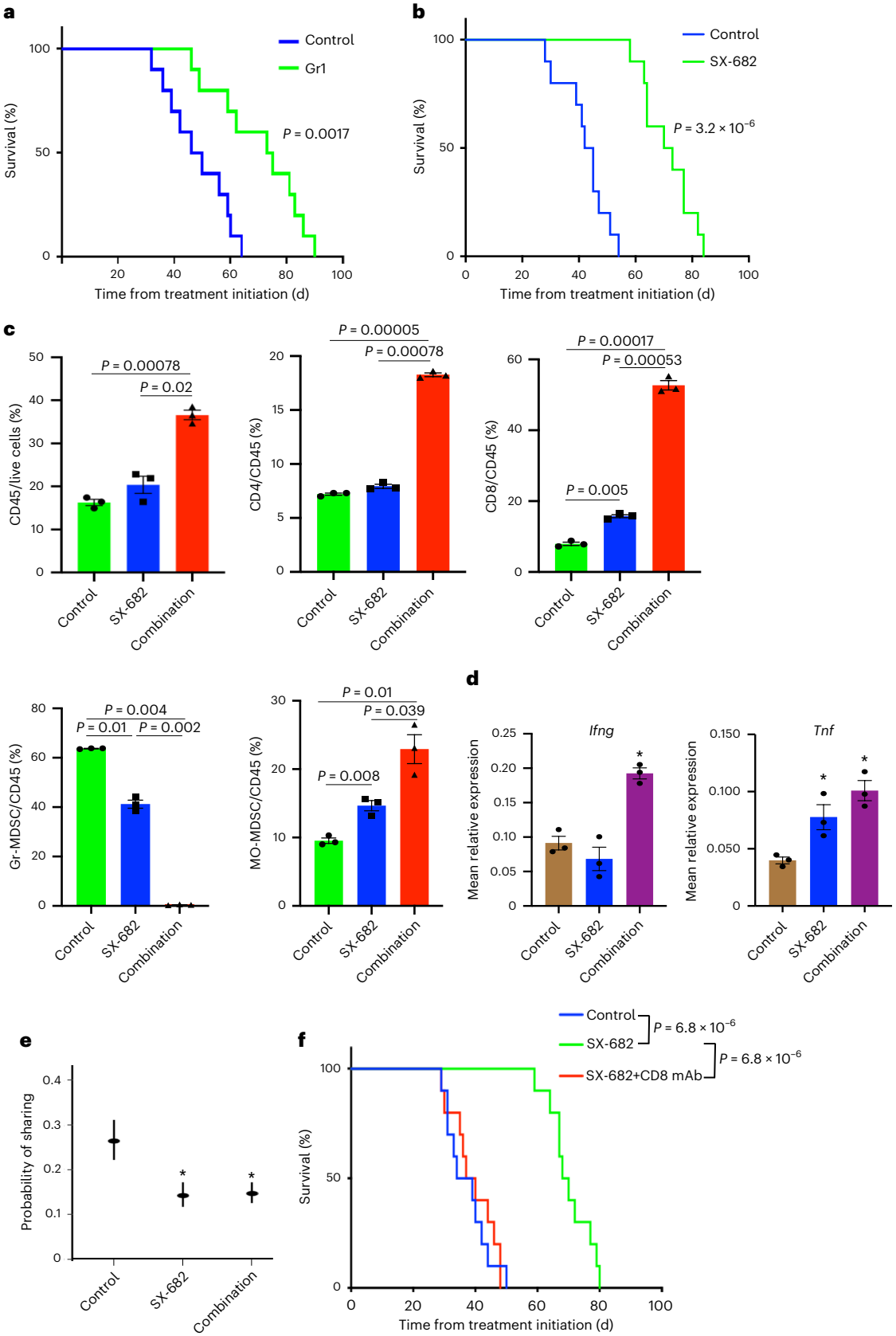

https://doi.org/10.1038/s43018-022-00500-z

These $CD3^+CD4^-CD8^-$ cells are characterized by high interleukin-17 (IL-17) expression and accounted for ~75% of the total $IL\text{-}17^+$ immune cells in iKRAS tumors (Fig. 6f)[53]. They displayed higher CCR7 expression compared with $CD4^+$ and $CD8^+$ T cells, consistent with previous studies[53] (Extended Data Fig. 8e). A higher proportion of $CD3^+CD4^-CD8^-$ T cells displayed CCR7 expression compared with $CD4^+$ and $CD8^+$ T cells, while a lower proportion of $CD3^+CD4^-CD8^-$ T cells displayed IL-2Rβ expression compared with $CD4^+$ and $CD8^+$ T cells, as described previously[53] (Extended Data Fig. 8f). These $CD3^+CD4^-CD8^-$ cells express CCR2, which facilitates their recruitment to the PDAC TIME (Extended Data Fig. 8g)[53]. They express the adhesion ligand JAML (*Amica1*), the cytotoxic marker CD107a (*Lamp1*), STAT1, transforming growth factor-β and tumor necrosis factor (TNF) and have minimal IL-10 expression, consistent with their immunogenic functions (Extended Data Fig. 8g). They also express *Ccl5*, which can reprogram myeloid cells toward antitumor immunity (Extended Data Fig. 8g)[53].

ICT can remodel both T cell and myeloid compartments in the TIME[22]. Correspondingly, effective ICT agents (antagonist LAG3 and agonist 41BB) decreased immunosuppressive neutrophils/granulocytes, whereas ineffective ICT agents (antagonists PD-1 and CTLA4) resulted in an increase (Fig. 5f and Extended Data Fig. 7d). LAG3 treatment also stimulated myeloid cell reprogramming, including upregulation of antigen presentation genes (*H2-Ab1*, *H2-Aa*, *CD74* and *β2m*; Fig. 6g) and downregulation of M2-associated transcription factors (*Stat6*, *Socs3* and *IL1β*) (Extended Data Fig. 8h). 41BB treatment reprogrammed myeloid cells by increasing antigen presentation gene expression (*H2-Ab1*, *H2-aa*, *CD74* and *β2m*; Fig. 6g), upregulating genes related to T cell chemoattraction (*Cxcl10*) and IFN signaling (*Stat1*) (Extended Data Fig. 8i) and downregulating genes/ transcription factors driving M2-polarization (*CD206*, *IL10* and *Socs3*) (Extended Data Fig. 8i).

Treatment with both effective and ineffective ICT agents resulted in a modest increase in dendritic cells compared with control treatment (Fig. 5f and Extended Data Fig. 7d). Treatment with LAG3 resulted in increased B cells, while PD-1 and CTLA4 treatment resulted in decreased B cells, consistent with previous studies showing that B cell infiltration is associated with better prognosis in PDAC[56] and may promote immunotherapy response[57]. In summary, 41BB and LAG3 treatment promote antitumor immunity by modulating T cell subsets with antitumor activity, increasing T cell clonality and diversification, decreasing immunosuppressive myeloid cells and increasing antigen presentation and decreasing the immunosuppressive capability of myeloid cells. However, this dual ICT combination was not sufficient to induce durable complete elimination of established tumors (Fig. 5c,d), suggesting the need to target additional immune-suppressive mechanisms in the iKRAS TIME.

Targeting CXCR2 expressed on MDSCs in iKRAS tumors

Increased frequency of MDSCs in the bone marrow, circulation and TIME correlates with advanced disease stage and poor survival in patients with PDAC[14,15,58,59]. In human PDAC, unsupervised clustering analysis of the 39-gene MDSC signature[13] categorized 178 TCGA primary PDAC tumors into MDSC-high ($n = 114$), -medium ($n = 54$) and -low ($n = 10$) groups (Extended Data Fig. 2b), revealing that MDSC-high patients showed significantly lower overall survival compared with MDSC-low patients (Extended Data Fig 9a). These clinical correlations, coupled with abundant MDSCs in iKRAS PDAC tumors (Fig. 1c–e and Extended Data Fig. 1g,h) prompted exploration of the impact of MDSC neutralization in iKRAS PDAC tumor progression. Using a well-characterized anti-Gr1 neutralizing antibody[13], treatment of mice with established iKRAS tumors depleted MDSCs (decreased S100A9 expression) (Extended Data Fig. 9b), increased intratumoral $CD8^+$ T cells (Extended Data Fig 9b), impaired tumor progression and increased overall survival, although all mice eventually succumbed (Fig. 7a and Extended Data Fig. 9c).

CXCR2 is highly expressed in the myeloid_c2 and myeloid_c3 clusters of untreated iKRAS tumors (Extended Data Fig. 3d,e) and in sorted granulocytic/neutrophilic MDSCs (Extended Data Fig. 9d), mirroring treatment-naive human PDAC specimens where CXCR2 is coexpressed with CD15 on $CD11b^+$ myeloid cells (Extended Data Fig. 9e). Similarly, scRNA-seq of 16 treatment-naive human patients with PDAC showed CXCR2 expression in granulocytes/neutrophils (Extended Data Fig. 9f)[10]. In comparison, CSF1R, CCR2 and TREM2 are predominantly expressed on the macrophages/monocytes in human PDAC and iKRAS tumors (Extended Data Figs. 7c and 9f). These CXCR2 expression profiles, coupled with its key role in MDSC recruitment to tumors[60], prompted evaluation of a clinical-stage Cxcr1/2 inhibitor, SX-682. Treatment with SX-682 significantly decreased migration of MDSCs isolated from iKRAS tumors toward conditioned medium in vitro (Extended Data Fig. 9g), inhibited tumor growth and increased the overall survival of tumor-bearing iKRAS mice, although all mice eventually succumbed (Fig. 7b and Extended Data Fig. 9h). Flow cytometry and confirmatory IHC analysis of iKRAS tumors following 4 weeks of SX-682 treatment showed decreased intratumoral $CXCR2^+$ granulocytic MDSCs and increased $CD8^+$ T cell infiltrate (Fig. 7c and Extended Data Fig. 9i–l), as well as modestly increased dendritic cell infiltration and no significant change in TAM infiltration (Extended Data Fig. 9j). SX-682 treatment resulted in a significant increase in the effector memory phenotype of both $CD4^+$ and $CD8^+$ T cells (Extended Data Fig. 9i). Consistent with previous studies[59,61], reduced $CXCR2^+$ neutrophilic/granulocytic MDSCs were associated with a reciprocal increase in monocytic MDSCs by flow cytometry (Fig. 7c) and scRNA-seq, with an increase in cluster M_c2 (*S100a4*-, *S100a6*-, *Ly6c2*- and *Ccr2*-expressing monocytic MDSCs) (Extended Data Fig. 9m). SX-682 treatment resulted in increased TNF expression by T cells, but no change in IFN-γ expression (Fig. 7d), as well as increased TCR diversification (Fig. 7e). We performed $CD8^+$ T cell depletion in the SX-682 trial, showing loss of tumor inhibition and survival benefit, indicating that the therapeutic effects of SX-682 are mediated by $CD8^+$ T cells (Fig. 7f and Extended Data Fig. 9n).

Fig. 8 | Efficacy of ICT in combination with targeted therapy directed against Cxcr1/2 and treatment effects on the immune microenvironment. **a**, Overall survival of mice bearing established orthotopic iKRAS tumors (tumor volume = ~250 mm^3 before treatment initiation) treated with control, anti-LAG3 + anti-41BB or anti-LAG3 + anti-41BB + SX-682 for 4 weeks ($n = 10$ mice per group). **b**, Changes in the fraction of cells in clusters T_c2, T_c3, T_c4 and T_c5 as a proportion of total T cells in scRNA-seq analysis of iKRAS tumors following treatment with the control or combination therapy (anti-LAG3 + anti-41BB + SX-682) for 4 weeks ($n = 3$ tumors per group). **c**, Relative expression of effector, memory, naive and exhausted signatures[62] in T cells from scRNA-seq analysis of iKRAS tumors after combination treatment (anti-LAG3 + anti-41BB + SX-682) for 4 weeks compared with the control ($n = 3$ tumors per group). $^*P < 0.05$. Values in the median score axis refer to the three innermost concentric rings. **d**, Overall survival of mice bearing established orthotopic iKRAS tumors (tumor volume = ~250 mm^3 before treatment initiation) treated with control, anti-PD-1 + anti-CTLA4 antibodies, SX-682 or anti-PD-1 + anti-CTLA4 + SX-682 for 4 weeks ($n = 10$ mice per group). **e**, Overall survival of mice bearing established orthotopic iKRAS tumors (tumor volume = ~250 mm^3 before treatment initiation) that were cured (survival > 6 months after treatment discontinuation) by the combination in **a** (anti-LAG3 + anti-41BB + SX-682) rechallenged with secondary tumors ($n = 5$ mice per group). Treatment-naive mice were animals who had never been exposed to iKRAS cells previously. **f**, Overall survival of mice bearing established autochthonous iKRAS tumors (tumor volume = ~250 mm^3 before treatment initiation) treated with control, anti-PD-1 + anti-CTLA4 antibodies, anti-LAG3 + anti-41BB antibodies, SX-682 or anti-LAG3 + anti-41BB + SX-682 for 4 weeks ($n = 10$ mice per group). Animals in the LAG3 + 41BB + SX-682 extended treatment group received extended treatment with the combination regimen for 6 months or until death. Statistical significance was determined by Kaplan–Meier survival curves and log-rank test (**a**,**d**–**f**), mixed-effect model (**b**) or two-sided unpaired Wilcox test (**c**). The data in **b** are presented as means ± s.e.m.

https://doi.org/10.1038/s43018-022-00500-z

These findings are consistent with previous studies, which showed a critical role for Cxcr2 signaling in the myeloid compartment in mediating PDAC tumorigenesis, antitumor immunity and chemotherapeutic response[28,61]. Together, these findings suggest that, similar to targeting exhausted T cells with ICT agents (41BB and LAG3), targeting myeloid cells alone is of transient benefit.

Combination immunotherapy renders iKRAS tumors curable

The above findings prompted combined ICT and CXCR2 inhibitor therapy, producing complete regression of established orthotopic iKRAS tumors in all mice (Fig. 8a and Extended Data Fig. 10a). The response was durable, with 90% mice still alive at 18 months after discontinuation of treatment, without evidence of relapse (Fig. 8a). From a mechanistic standpoint, flow cytometry and IHC analyses showed that the triple combination of 41BB agonist, LAG3 antagonist and SX-682 resulted in near-complete depletion of intratumoral CXCR2$^+$ granulocytic/neutrophilic MDSCs and an associated marked increase in CD8$^+$ and CD4$^+$ T cell infiltrates (Fig. 7c and Extended Data Fig. 9i–l). Correspondingly, scRNA-seq showed increased T_c2 (high *GzmK*, high *GzmB* and high *Ccl5* activated CD4$^+$ T cells) and T_c3 clusters (high *GzmK*,

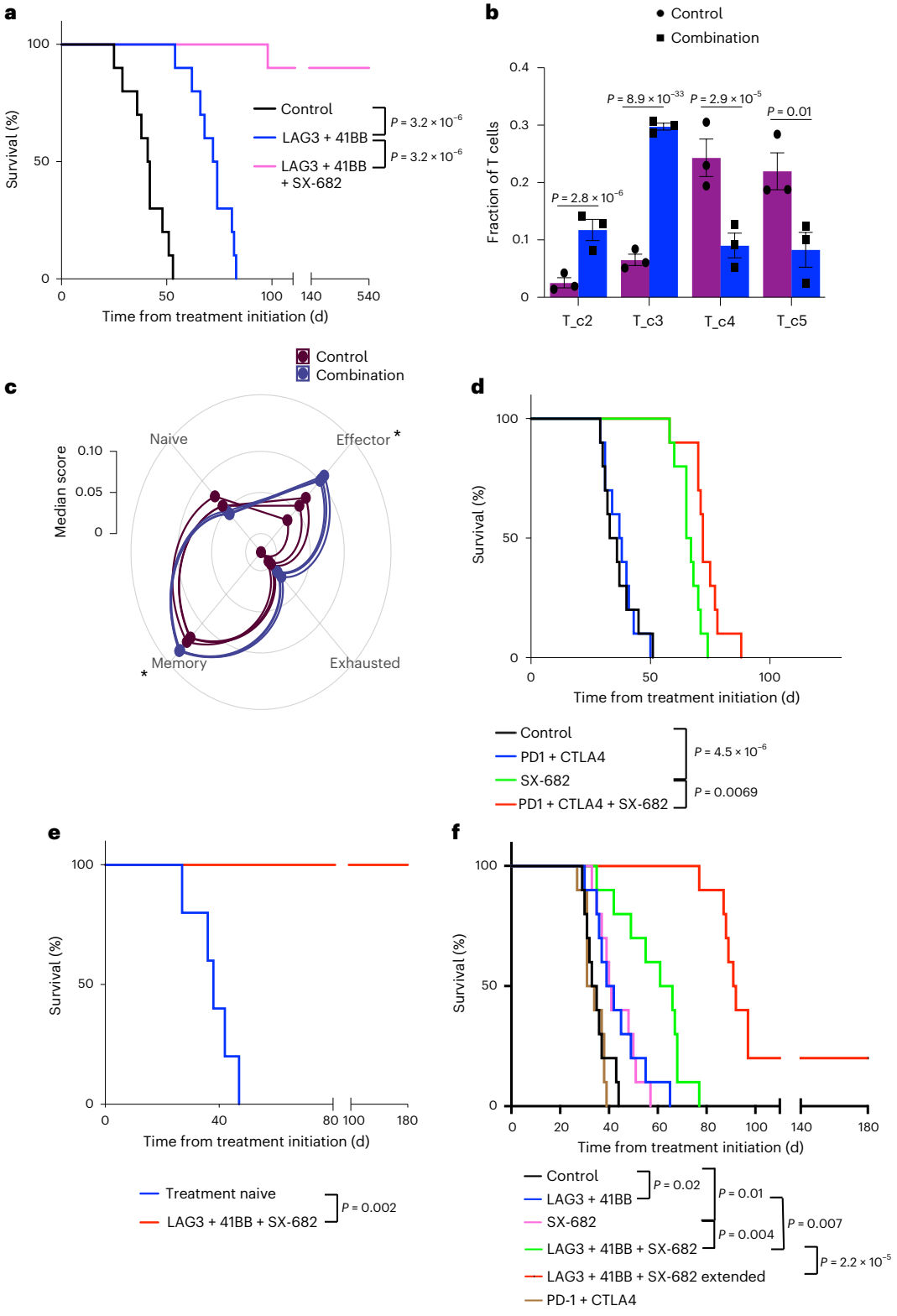

low *GzmB* and high *Ccl5* activated CD8$^+$ T cells) and decreased naive or central memory CD4$^+$ (cluster T_c5) and CD8$^+$ (cluster T_c4) T cells (Fig. 8b). Triple therapy resulted in higher TNF and IFN-γ expression by T cells (Fig. 7d) and increased the effector memory phenotype of infiltrating CD4$^+$ and CD8$^+$ T cells (Extended Data Fig. 9i). scRNA-seq analysis of T cells validated that triple therapy induced increased effector and memory signatures compared with the control treatment (Fig. 8c)[62]. There was a modest increase in dendritic cell infiltration (Extended Data Fig. 9j) and no significant change in TAM infiltration (Extended Data Fig. 9j), consistent with the finding that CXCR1/2 inhibition selectively targets MDSCs. We noted that depletion of CXCR2$^+$ neutrophilic/granulocytic MDSCs results in a compensatory increase in monocytic MDSCs, similar to SX-682 monotherapy treatment (Fig. 7c). scRNA-seq confirmed a significant increase in the M_c2 cluster fraction (*S100a4*-, *S100a6*-, *Ly6c2*- and *Ccr2*-expressing monocytic MDSCs) (Extended Data Fig. 9m). The increase in monocytic MDSCs after combination treatment did not impact CD4$^+$/CD8$^+$ T cell infiltration or activity or the therapeutic efficacy of the combination regimen, given durable, complete responses up to 18 months after discontinuation of combination treatment (Fig. 8a and Extended Data Fig. 10a), suggesting that monocytic MDSCs are unable to fully substitute for the immune-suppressive activity of neutrophilic/granulocytic MDSCs in the iKRAS model. Treatment with the combination also resulted in TCR diversification, consistent with the effects noted with 41BB agonist, LAG3 antagonist and SX-682 monotherapies (Fig. 7e). In contrast, the SX-682, anti-PD-1 and anti-CTLA4 combination treatment resulted in a modest decrease in tumor size along with increased survival, although none of the mice cleared their tumors following therapy and there were no durable responses noted (Fig. 8d and Extended Data Fig. 10b). These findings highlight the profound antitumor activity of the combination of 41BB agonist, LAG3 antagonist and SX-682, revealing that specific checkpoint combinations synergize with CXCR2 inhibition in the iKRAS model. Moreover, triple therapy was well tolerated with no treatment-related deaths during the 4-week treatment period and nine out of ten mice survived for >18 months after treatment discontinuation (Fig. 8a). Transient elevation in liver function tests (aspartate transaminase and alanine aminotransferase) was noted, consistent with the previously described hepatotoxicity related to 41BB antibodies (Extended Data Fig. 10c)[63,64].

The effectiveness of triple therapy was further evidenced by tumor rechallenge studies, where 100% of the cured mice showed tumor rejection, consistent with a memory T cell response (Fig. 8e). Moreover, given that tumor cells with identical tumor-initiating genetic alterations may elicit variable immune infiltrates and differential responses to immunotherapy[65], the curative efficacy of triple therapy was confirmed in additional independently derived iKRAS cell lines, which exhibit different patterns of immune cell infiltration, specifically lower T cells and higher myeloid cells (Extended Data Fig. 10d–f). It is possible that the orthotopic model may not fully recapitulate the complex fibroblastic stroma that is characteristic of the autochthonous model or human PDAC. Therefore, we tested the efficacy of triple therapy in established autochthonous tumors in the iKRAS model, using the same dose and schedule as the orthotopic iKRAS PDAC studies (Extended Data Fig. 10g). Consistent with findings from the orthotopic model and human clinical trials[7], the combination of antagonist PD-1 and CTLA4 antibodies had no appreciable effects, whereas triple therapy increased the survival of iKRAS genetically engineered mouse model (GEMM) mice (Fig. 8f). We also evaluated the effects of extended dosing (that is, continuous dosing beyond 28 d) with the triple therapy regimen to examine whether it could result in durable remissions (Extended Data Fig. 10g). We found that two out of ten mice had a durable response lasting >6 months with extended dosing with the triple therapy regimen (Fig. 8f). Upon necropsy, these surviving mice had no evidence of primary tumor in the pancreas or metastases in the liver or lung, consistent with disease eradication.

Discussion

In this study, high-dimensional immune profiling of human and mouse PDAC was used to guide the development of an effective combination immunotherapy regimen, leading to unprecedented complete, durable responses and markedly improved survival in the treatment-resistant iKRAS PDAC model. In contrast with anti-PD-1 and anti-CTLA4, agonist 41BB and antagonist LAG3 treatment reprogrammed the TIME toward antitumor immunity with increased T cell subsets with antitumor effects, increased T cell clonality and diversification, decreased immunosuppressive myeloid cells and increased antigen presentation and decreased the immunosuppressive capability of remaining myeloid cells. The addition of therapy targeting CXCR1/2 on neutrophilic/granulocytic MDSCs revealed that effective immune treatment is possible in PDAC but requires neutralization of distinct immunosuppressive mechanisms. Although we demonstrate reprogramming of MDSCs with SX-682 in mice, whether the same mechanisms govern myeloid cell migration into the TIME in human PDAC remains unknown.

As with all preclinical model systems and human biospecimen correlations, prospective clinical trials will be needed to substantiate the hypothesis generated from this work. Along these lines, it is notable that the expression of both 41BB and LAG3 is elevated on tumor-infiltrating T cells compared with circulating T cells in human PDAC[24], consistent with the validated expression of both 41BB and LAG3 on T cells in human PDAC. Moreover, we found that 81% of patients with PDAC have 41BB-expressing T cells, while 93% of patients with PDAC have LAG3-expressing T cells, suggesting that these targets may be relevant for a meaningful fraction of patients with PDAC. In this context, it is noteworthy that the majority of ongoing immunotherapy trials in PDAC employ PD-1 and/or CTLA4 as the ICT backbone, including trials combining ICT with CXCR2 antagonists[4].

Recent studies implicate the CD155–TIGIT axis in mediating immune evasion in PDAC, and human trials are ongoing to evaluate ICT antibodies targeting TIGIT[37]. Our findings suggest that ICT antibodies targeting 41BB and LAG3 also hold the potential to elicit meaningful responses in patients with PDAC. More specifically, the tumor shrinkage and radiographic responses in all orthotopic or autochthonous tumors treated with triple therapy point to a window-of-opportunity trial for surgical resection in patients with previously unresectable primary tumors due to involvement of nearby blood vessels, lymph nodes or organs (such as the duodenum). Moreover, the cures noted in orthotopic tumors and the significant improvement in overall survival and durable remissions noted in autochthonous iKRAS tumors indicate that this lethal cancer can be rendered vulnerable to combination immunotherapy.

Methods

Transgenic and syngeneic mouse studies

All of the animal work performed in this study was approved by the MD Anderson and Rutgers Institutional Animal Care and Use Committee. All animals were maintained under pathogen-free conditions and cared for in accordance with the Association for Assessment and Accreditation of Laboratory Animal Care International policies and certification. iKRAS (p48-Cre; tetO_LSL-Kras^{G12D}; ROSA_rtTA; p53$^{L/+}$) genetically engineered mice were described previously and were backcrossed to the C57BL/6 background for more than eight generations to achieve a pure B6 mouse to generate syngeneic cell lines[8]. Female or male mice were administered doxy water (2 mg/ml doxycycline and 40 mg/ml sucrose) starting at 4 weeks of age to activate transgenic KRAS^{G12D} expression. For orthotopic pancreas transplantation, C57BL/6 female or male mice aged 5–7 weeks (The Jackson Laboratory) were anesthetized using ketamine and xylazine. An incision was made in the left abdomen and the pancreas was gently pulled out along with the spleen. iKRAS cells were slowly injected into the tail of the pancreas using a Hamilton syringe. Cells (5×10^5 in 5 µl) mixed with 5 µl Matrigel were injected. Analgesic was administered after surgery, along with temperature-controlled

postsurgical monitoring. Doxycycline was provided to the animals in the form of doxy water (2 mg/ml doxycycline and 40 mg/ml sucrose) starting on the day of tumor cell injection. Animals were imaged (IVIS Spectrum (PerkinElmer) and ICON MRI (Bruker)) 10 d after surgery to assess the successful implantation of tumors. Only tumors of similar volume (~250 mm^3) were used for treatment studies. Animals underwent MRI imaging to monitor the progression of the tumors. Mice with autochthonous PDAC tumors were euthanized for tumor collection once the tumor volume was approximately the same as that of orthotopic tumors (~1,000 mm^3). Owing to the retroperitoneal location of PDAC tumors, we used signs of lethargy, reduced mobility and morbidity, rather than maximum tumor size, as a protocol-enforced endpoint.

Noninvasive mouse imaging

For MRI imaging with the Bruker ICON, animals were anesthetized with 1–3% isoflurane and placed on the ICON animal bed. The MRI coil was secured into position over the animals and the entire bed assembly was placed into the Bruker ICON MRI bore. Rapid acquisition with relaxation enhancement T2-weighted images were acquired in coronal, sagittal and axial planes. The coronal and sagittal T2 parameters were as follows: echo time = 18 ms, repetition time = 2,197 ms, slice thickness = 1 mm and slice gap = 1.25 mm. The axial T2 parameters were as follows: echo time = 14.2 ms, repetition time = 1.464 ms, slice thickness = 1.25 mm and slice gap = 1.5 mm. After imaging was completed, the animals were allowed to recover under a heating lamp until fully conscious. MRI images were loaded into ImageJ to manually demarcate the contour of the pancreas and calculate the total volume. Bioluminescence imaging with the IVIS Spectrum (PerkinElmer) was performed by intraperitoneal injection of 1.5 mg D-luciferin (PerkinElmer). The Living Image 4.7 software (PerkinElmer) was used for analysis of images postacquisition. Positron emission tomography was performed using a Bruker Albira PET/CT scanner 1 h after injection of ~150 µCi ^{18}FDG. The respiratory rate was monitored with a BIOPAC physiological monitoring system used to gate the computed tomography results.

CyTOF analysis of mouse and human tumors

Tumor cells were isolated from iKRAS tumors using the Mouse Tumor Dissociation Kit (Miltenyi Biotec). A total of five patients with PDAC who were undergoing pancreatectomy were recruited at the MD Anderson Cancer Center through informed written consent following Institutional Review Board approval. All patients consented to participation with publication of deidentified data. Pancreatic tissue was delivered to the laboratory on ice after surgical resection in Dulbecco's modified Eagle medium in a 15 ml conical tube. Tumor cells were isolated from human PDAC tumors using the Human Tumor Dissociation Kit (Miltenyi Biotec). Single cells were isolated from tumors using a standard protocol and as described previously[13,18]. All isolated cells were depleted of erythrocytes by hypotonic lysis. For CyTOF analysis, cells were blocked for FcγR for 10 min and incubated with CyTOF antibody cocktail mix (see Supplementary Table 2 for a list of the antibodies) for 30 min at room temperature. Cells were washed once and incubated with Cell-ID Cisplatin (Fluidigm) at 2.5 µM for 2 min for viability staining. Cells were fixed with Maxpar Fix and Perm Buffer containing Cell-ID Intercalator-Ir (Fluidigm) at 0.125 µM and incubated at 4 °C overnight to stain the nuclei. The samples were analyzed using a CyTOF instrument (Fluidigm) in the Flow Cytometry and Cellular Imaging Core Facility at the MD Anderson Cancer Center. Data were analyzed with FlowJo (Tree Star) and SPADE software.

Flow cytometry analysis

Single cells were obtained as described above for CyTOF. To assess cell viability, cells were incubated with Ghost Dye Violet (Tonbo Biosciences) for 15 min in the dark and then stained with the indicated antibodies for 30 min on ice before fluorescence-activated cell sorting analysis. Fluorochrome-conjugated antibody information is listed in the reporting summary. For FOXP3 staining, cells were fixed and permeabilized (eBioscience FOXP3/Transcription Factor Staining Buffer Set) and stained with FOXP3. All samples were acquired with the FACSAria Fusion sorter (BD Biosciences) and analyzed with FlowJo software (Tree Star).

T cell suppression and MDSC migration assay

MDSCs were isolated from the spleens of iKRAS mice using a Mouse Myeloid-Derived Suppressor Cell Isolation Kit (Miltenyi Biotec) and plated in RPMI 1640 supplemented with 10% fetal bovine serum and antibiotics. MDSCs (1×10^5 cells per well) were seeded in the top chamber of the transwell (Corning). Conditioned media from cultured iKRAS cells was collected and added to the bottom layer of the transwell. After 4 h incubation, cells that had completely migrated to the bottom chamber were counted. A T cell suppression assay was performed as described previously[13,18] using equal numbers of MACS-sorted MDSCs and carboxyfluorescein succinimidyl ester (CFSE) (Invitrogen)-labeled, MACS-sorted (Miltenyi Biotec) $CD8^+$ T cells in anti-CD3- and anti-CD28-coated 96-well plates at MDSC/T cell ratios of 0:1, 1:1 and 4:1 with 5.0×10^5 MDSCs. MDSCs were isolated from iKRAS tumors and $CD8^+$ T cells were isolated from the spleen of C57BL/6 mice (The Jackson Laboratory). The CFSE intensity was quantified 72 h later with peaks identified using a BD LSRFortressa Cell Analyzer. CFSE peaks indicated the T cell division times. High and low proliferation were defined as T cell divisions of ≥2 and ≤1, respectively.

Multiplex immunofluorescence staining

Multiplex immunofluorescence staining was performed as described and validated previously[66]. Briefly, four micrometer-thick, formalin-fixed, paraffin-embedded tissue sections were stained using panels containing the antibodies outlined in the reporting summary. All of the markers were stained in sequence using their respective fluorophores in the Opal 7 kit (Akoya Biosciences/PerkinElmer). The stained slides were scanned using a multispectral microscope (Vectra 3.0.3 imaging system; Akoya Biosciences/PerkinElmer) under fluorescence conditions at low magnification (10×). After scanning at low magnification, each core was scanned at high magnification (20×) and analyzed by a pathologist using InForm 2.4.0 image analysis software (Akoya Biosciences/PerkinElmer). Marker colocalization was used to identify specific cell phenotypes ($CD33^+CD11b^+CD66b^+$, $CD33^+CD14^+CD68^+$, $CD3^+41BB^+$, $CD3^+LAG3^+$, $CD3^+CD8^+CD45RO^+$ and $CD3^+CD8^+GzmB^+$). All of the data were consolidated using RStudio 3.5.3 (Phenopter 0.2.2 packet; Akoya Biosciences/PerkinElmer) and SAS Enterprise 7.1.

Cell lines

iKRAS (p48-Cre; tetO_LSL-$Kras^{G12D}$; ROSA_rtTA; $p53^{L/+}$) syngeneic cell lines have been described previously[8]. Cells were maintained in culture in RPMI medium supplemented with 10% fetal bovine serum and doxycycline. All cell lines were tested for *Mycoplasma* and found to be negative within 3 months of performing the experiments.

IHC

Human PDAC samples were obtained from MD Anderson's Tissue Biobank. Human studies were approved by MD Anderson's Institutional Review Board and previous informed consent was obtained from all participants under IRB protocol LAB05-0854. Mouse tissues were fixed in 10% formalin overnight and embedded in paraffin. Immunohistochemical staining was performed as described previously[13]. Slides were scanned using an Aperio AT2 slide scanner (Leica Biosystems). Images were visualized and a pathologist selected regions of interest (tumor or normal pancreas); necrotic areas and areas with artifact were excluded from the analysis. Primary antibodies for mouse and human tissue staining are listed in the reporting summary.

ICT, chemotherapy and targeted therapy

For in vivo pharmacological inhibition, gemcitabine (Selleck Chemicals) was dosed at 100 mg/kg intraperitoneally. SX-682 (Syntrix Pharmaceuticals) was dosed orally ad libitum (with a formulated concentration of 714 mg/kg feed). Therapeutic plasma levels (range = 0.5–10 µg/ml were confirmed with this feed using liquid chromatography with tandem mass spectrometry. For ICT and Gr1/CD8-neutralizing antibody treatment, anti-PD-1 (clone RMP1-14; BE0146; BioXCell), anti-CTLA4 (clone 9H10; BE0131; BioXCell), anti-TIM3 (clone RMT3-23; BE0115; BioXCell), anti-OX40 (clone OX-86; BE0031; BioXCell), anti-41BB (clone LOB12.3; BE0169; BioXCell), anti-LAG3 (clone C9B7W; BE0174; BioXCell), anti-CD8 (clone 2.43; BE0061; BioXCell) and anti-Gr1 (clone RB6-8C5; BE0075; BioXCell) antibodies (or their respective isotype immunoglobulin G controls) were intraperitoneally administered at 200 µg per injection three times per week. The duration of treatment was 4 weeks before endpoint analysis and survival analysis unless otherwise indicated.

Computational analysis of human PDAC TCGA, ICGC and scRNA-seq data

For TCGA gene set enrichment analysis, the TCGA PDAC messenger RNA dataset, gene mutations and clinical survival data were downloaded from the TCGA website. For ICGC gene set enrichment analysis, the ICGC PDAC-AU messenger RNA dataset, gene mutations and clinical survival data were downloaded from the ICGC (International Cancer Genome Consortium) data portal. For analysis of human PDAC data, we utilized a 39-gene human MDSC signature, which was described previously[13]. The gene expression data of 178 TCGA PDAC samples were clustered using the 39 MDSC genes into MDSC-high, MDSC-low and MDSC-medium (the distance between pairs of samples was measured by Manhattan distance and clustering was then performed using complete-linkage hierarchical clustering). Similarly, normalized gene expression data from PDAC TCGA (178 samples) or ICGC-AU (92 samples) were used to infer the relative proportions of infiltrating immune cells using the CIBERSORTx algorithm, which was described previously[16]. Estimated fractions of each immune cell subset were related to survival using univariate Cox regression. Two human PDAC scRNA-seq cohorts were used from Peng et al.[26] and Steele et al.[10]. For the Peng et al. cohort, original cell type annotations of scRNA clusters were used. For the Steele et al. cohort, data were processed and clustered according to the R scripts from the original paper. UMAP clusters were further annotated using the rSuperCT algorithm[67]. The expression of selected marker genes was compared among different cell types. All data processing and analysis was implemented in the R 4.0.5 environment and Seurat package version 4.0.1.

scRNA-seq, transcriptomic and TCR analysis of mouse tumors

Flow cytometry to isolate live CD45$^+$ cells was performed using a standard protocol as noted above for the FACSAria Fusion sorter (BD Biosciences) and analyzed with FlowJo software (Tree Star). Live CD45$^+$ cells were processed with the 10X Genomics Chromium platform, with the 5′ V(D)J solution chemistry, per the manufacturer's protocol. TCR sequences were enriched with the primers listed below, and the resulting libraries were pooled and 150-base pair paired end sequenced on the Illumina MiSeq with the V2 300-cycle kit. Single-cell transcriptome libraries were pooled and 26–91 base pair paired end sequenced on the NovaSeq S2 system to a targeted depth of 100,000 reads per cell. Raw sequencing data were processed through the 10X Genomics Cell Ranger version 2.1.0 pipeline and then analyzed in R. Cells were detected using the DropletUtils package[68] with a false discovery rate of 0.01, and barcode swapped counts were removed using swappedDrops. Supernatant RNA contamination was filtered using the package SoupX[69]. Data were then processed using the Seurat package[70]. Cells with a mitochondrial gene percentage of >15% were filtered and samples were corrected for batch effects by aligning the first 35 canonical correlations using the MultiCCA function. Cells were clustered with SNN. Differences in cluster fractions were assessed by the significance of treatment as a fixed effect in a binomial mixture model (glmer in the lme4 R package) with replicate included as a random effect. Pseudotime analysis was performed using the Monocle2 package per the recommended workflow[34]. To determine the lineage of each individual T cell in the PDAC tumors after the various ICT treatments, we designed primers for the mouse α and β TCR locus and performed targeted PCR on the 10X Genomics single-cell 5′ complementary DNA product (Supplementary Table 4). From the TCR product library, we assembled the full-length TCR α and β sequences. Raw TCR sequencing data were processed through the 10X Genomics cellranger vdj version 2.1.0 pipeline. Clonotypes where only an α or β chain was detected, but that exactly matched the arCDR3 nucleotide sequence from an α–β paired clonotype were combined into the paired clonotype for further analysis.

Statistics and reproducibility

Continuous measurements were compared pairwise using a two-sample Student's *t*-test. The data are presented as means ± s.d. unless otherwise indicated. Measures expressed as percentages were transformed (to improve normality) via a logit transformation before using Student's *t*-tests. Survival outcomes were compared using log-rank tests and Kaplan–Meier survival curves. In the case of multiple pairwise comparisons, Benjamini–Hochberg adjusted *P* values were reported[71]. Figs. 2a,b and 5e show representative images from a total of $n = 54$ patients.

Transgenic and syngeneic mouse experiments were randomized and investigators were blinded to allocation during the experiments and outcome assessment. No statistical method was used to predetermine sample size. The animal cohort sizes for the study were estimated based on previous experience using similar mouse models that showed significance. No animals or data points were excluded from the analyses. Data distribution was assumed to be normal but this was not formally tested.

Changes in the average relative expression or expression of gene signature scores, as determined by scRNA-seq, were analyzed by two-sided unpaired Wilcox test. For single-cell populations, differences in cluster fractions were assessed by the significance of treatment as a fixed effect in a binomial mixture model (glmer in the lme4 R package) with sample replicate included as a random effect.

Reporting summary

Further information on research design is available in the Nature Portfolio Reporting Summary linked to this article.

Data availability

Murine scRNA-seq and TCR sequencing data supporting the findings of this study have been deposited in the Sequence Read Archive under BioProject accession code PRJNA496487. Human PDAC genomic data were derived from the TCGA Research Network (http://cancergenome.nih.gov) and ICGC Research Network (https://dcc.icgc.org). Human PDAC scRNA-seq data were derived from the Genome Sequence Archive (accession codes CRA001160 and GSE155698). All of the other data are available from the corresponding authors upon reasonable request. Source data are provided with this paper.

References

1. Siegel, R. L., Miller, K. D., Fuchs, H. E. & Jemal, A. Cancer statistics, 2022. *Cancer J. Clin.* **72**, 7–33 (2022).
2. Ying, H. et al. Genetics and biology of pancreatic ductal adenocarcinoma. *Genes Dev.* **30**, 355–385 (2016).
3. Rahib, L. et al. Projecting cancer incidence and deaths to 2030: the unexpected burden of thyroid, liver, and pancreas cancers in the United States. *Cancer Res.* **74**, 2913–2921 (2014).
4. Bear, A. S., Vonderheide, R. H. & O'Hara, M. H. Challenges and opportunities for pancreatic cancer immunotherapy. *Cancer Cell* **38**, 788–802 (2020).

5. Brahmer, J. R. et al. Safety and activity of anti-PD-L1 antibody in patients with advanced cancer. *N. Engl. J. Med.* **366**, 2455–2465 (2012).
6. Royal, R. E. et al. Phase 2 trial of single agent Ipilimumab (anti-CTLA-4) for locally advanced or metastatic pancreatic adenocarcinoma. *J. Immunother.* **33**, 828–833 (2010).
7. O'Reilly, E. M. et al. Durvalumab with or without tremelimumab for patients with metastatic pancreatic ductal adenocarcinoma. *JAMA Oncol.* **5**, 1431–1438 (2019).
8. Ying, H. et al. Oncogenic Kras maintains pancreatic tumors through regulation of anabolic glucose metabolism. *Cell* **149**, 656–670 (2012).
9. Elyada, E. et al. Cross-species single-cell analysis of pancreatic ductal adenocarcinoma reveals antigen-presenting cancer-associated fibroblasts. *Cancer Discov.* **9**, 1102–1123 (2019).
10. Steele, N. G. et al. Multimodal mapping of the tumor and peripheral blood immune landscape in human pancreatic cancer. *Nat. Cancer* **1**, 1097–1112 (2020).
11. Bjornson, Z. B., Nolan, G. P. & Fantl, W. J. Single-cell mass cytometry for analysis of immune system functional states. *Curr. Opin. Immunol.* **25**, 484–494 (2013).
12. Bronte, V. et al. Recommendations for myeloid-derived suppressor cell nomenclature and characterization standards. *Nat. Commun.* **7**, 12150 (2016).
13. Wang, G. et al. Targeting YAP-dependent MDSC infiltration impairs tumor progression. *Cancer Discov.* **6**, 80–95 (2016).
14. Vayrynen, S. A. et al. Composition, spatial characteristics, and prognostic significance of myeloic cell infiltration in pancreatic cancer. *Clin. Cancer Res.* **27**, 1069–1081 (2021).
15. Liudahl et al. Leukocyte heterogeneity in pancreatic ductal adenocarcinoma: phenotypic and spatial features associated with clinical outcome. *Cancer Discov.* **11**, 2014–2031 (2021).
16. Newman, A. et al. Determining cell type abundance and expression from bulk tissues with digital cytometry. *Nat. Biotechnol.* **27**, 773–782 (2019).
17. Zhang et al. Single-cell analyses inform mechanisms of myeloid-targeted therapies in colon cancer. *Cell* **181**, 442–459 (2020).
18. Lu, X. et al. Effective combinatorial immunotherapy for castration-resistant prostate cancer. *Nature* **543**, 728–732 (2017).
19. Blank, C. et al. Defining 'T cell exhaustion'. *Nat. Rev. Immunol.* **19**, 665–674 (2019).
20. Winograd, R. et al. Induction of T-cell immunity overcomes complete resistance to PD-1 and CTLA-4 blockade and improves survival in pancreatic carcinoma. *Cancer Immunol. Res.* **3**, 399–411 (2015).
21. Stromnes, I. M. et al. T-cell localization, activation, and clonal expansion in human pancreatic ductal adenocarcinoma. *Cancer Immunol. Res.* **5**, 978–991 (2017).
22. Gubin, M. M. et al. High-dimensional analysis delineates myeloid and lymphoid compartment remodeling during successful immune-checkpoint therapy. *Cell* **175**, 1014–1030 (2018).
23. Zilonis, R. et al. Single-cell transcriptomics of human and mouse lung cancers reveals conserved myeloid populations across individuals and species. *Immunity* **50**, 1317–1334 (2019).
24. Azizi, E. et al. Single-cell map of diverse immune phenotypes in the breast tumor microenvironment. *Cell* **174**, 1293–1308 (2018).
25. Hosein, A. N. et al. Cellular heterogeneity during mouse pancreatic ductal adenocarcinoma progression at single-cell resolution. *JCI Insight* **5**, e129212 (2019).
26. Peng, J. et al. Single-cell RNA-seq highlights intra-tumoral heterogeneity and malignant progression in pancreatic ductal adenocarcinoma. *Cell Res.* **29**, 725–738 (2019).
27. Chao, T., Furth, E. E. & Vonderheide, R. H. CXCR2-dependent accumulation of tumor-associated neutrophils regulates T-cell immunity in pancreatic ductal adenocarcinoma. *Cancer Immunol. Res.* **4**, 968–982 (2016).
28. Steele, C. W. et al. CXCR2 inhibition profoundly suppresses metastases and augments immunotherapy in pancreatic ductal adenocarcinoma. *Cancer Cell* **29**, 832–845 (2016).
29. Zhang, L. et al. Lineage tracking reveals dynamic relationships of T cells in colorectal cancer. *Nature* **564**, 268–272 (2018).
30. Andersson, K. M. et al. Survivin coordinates formation of follicular T-cells acting in synergy with Bcl-6. *Oncotarget* **6**, 20043–20057 (2015).
31. Sharief, M. K. & Semra, Y. K. Upregulation of the inhibitor of apoptosis proteins in activated T lymphocytes from patients with multiple sclerosis. *J. Neuroimmunol.* **119**, 350–357 (2001).
32. Miller, B. C. et al. Subsets of exhausted $CD8^+$ T cells differentially mediate tumor control and respond to checkpoint blockade. *Nat. Immunol.* **20**, 326–336 (2019).
33. Sade-Feldman, M. et al. Defining T cell states associated with response to checkpoint immunotherapy in melanoma. *Cell* **175**, 998–1013 (2018).
34. Trapnell, C. et al. The dynamics and regulators of cell fate decisions are revealed by pseudotemporal ordering of single cells. *Nat. Biotechnol.* **32**, 381–386 (2014).
35. Carstens, J. L. et al. Spatial computation of intratumoral T cells correlates with survival of patients with pancreatic cancer. *Nat. Commun.* **8**, 15095 (2017).
36. Balachandran, V. et al. Identification of unique neoantigen qualities in long-term survivors of pancreatic cancer. *Nature* **551**, 512–516 (2017).
37. Freed-Pastor, W. A. et al. The CD155/TIGIT axis promotes and maintains immune evasion in neoantigen expressing pancreatic cancer. *Cancer Cell* **39**, 1342–1360 (2021).
38. Rajeshkumar, N. V. et al. Superior therapeutic efficacy of *nab*-paclitaxel over cremophor-based paclitaxel in locally advanced and metastatic models of human pancreatic cancer. *Br. J. Cancer* **115**, 442–453 (2016).
39. Eriksson, E., Wenthe, J., Irenaeus, S., Loskog, A. & Ullenhag, S. Gemcitabine reduces MDSCs, Tregs and TGFβ-1 while restoring the Teff/Treg ratio in patients with pancreatic cancer. *J. Transl. Med.* **14**, 282 (2016).
40. Shevchenko, I. et al. Low-dose gemcitabine depletes regulatory T cells and improves survival in the orthotopic Panc02 model of pancreatic cancer. *Int. J. Cancer* **133**, 98–107 (2013).
41. Chihara, N. et al. Induction and transcriptional regulation of the co-inhibitory gene module in T cells. *Nature* **558**, 454–459 (2018).
42. Van Der Leun, A. M., Thommen, D. S. & Schumacher, T. N. $CD8^+$ T cell states in human cancer: insights from single cell analysis. *Nat. Rev. Cancer* **20**, 218–232 (2020).
43. Braun, D. A. et al. Progressive immune dysfunction with advancing disease stage in renal cell carcinoma. *Cancer Cell* **39**, 632–648 (2021).
44. Pollok, K. E. et al. Inducible T cell antigen 4-1BB. Analysis of expression and function. *J. Immunol.* **150**, 771–781 (1993).
45. Shuford, W. W. et al. 4-1BB costimulatory signals preferentially induce $CD8^+$ T cell proliferation and lead to the amplification in vivo of cytotoxic T cell responses. *J. Exp. Med.* **186**, 47–55 (1997).
46. Hernandez-Chacon, J. A. et al. Costimulation through the CD137/4–1BB pathway protects human melanoma tumor-infiltrating lymphocytes from activation-induced cell death and enhances antitumor effector function. *J. Immunother.* **34**, 236–250 (2011).
47. Sherwood, A. M. et al. Tumor-infiltrating lymphocytes in colorectal tumors display a diversity of T cell receptor sequences that differ from the T cells in adjacent mucosal tissue. *Cancer Immunol. Immunother.* **62**, 1453–1461 (2013).
48. Tumeh, P. C. et al. PD-1 blockade induces responses by inhibiting adaptive immune resistance. *Nature* **515**, 568–571 (2014).

49. Lawrence, M. S. et al. Mutational heterogeneity in cancer and the search for new cancer-associated genes. *Nature* **499**, 214–218 (2013).
50. Hopkins, A. C. et al. T cell receptor repertoire features associated with survival in immunotherapy-treated pancreatic ductal adenocarcinoma. *JCI Insight* **3**, e122092 (2018).
51. Manuel, M. et al. Lymphopenia combined with low TCR diversity (divpenia) predicts poor overall survival in metastatic breast cancer patients. *Oncoimmunology* **1**, 432–440 (2012).
52. Postow, M. A. et al. Peripheral T cell receptor diversity is associated with clinical outcomes following ipilimumab treatment in metastatic melanoma. *J. Immunother. Cancer* **3**, 23 (2015).
53. Hundeyin, M. et al. Innate αβ T cells mediate antitumor immunity by orchestrating immunogenic macrophage programming. *Cancer Discov.* **9**, 1288–1305 (2019).
54. Voelkl, S. et al. Characterization of MHC class-I restricted TCRαβ$^+$ CD4$^-$CD8$^-$ double negative T cells recognizing the gp100 antigen from a melanoma patient after gp100 vaccination. *Cancer Immunol. Immunother.* **58**, 709–718 (2009).
55. Young, K. J., Kay, L. S., Phillips, M. J. & Zhang, L. Antitumor activity mediated by double-negative T cells. *Cancer Res.* **63**, 8014–8021 (2003).
56. Castino, G. F. et al. Spatial distribution of B cells predicts prognosis in human pancreatic adenocarcinoma. *Oncoimmunology* **5**, e1085147 (2015).
57. Helmink, B. A. et al. B cells and tertiary lymphoid structures promote immunotherapy response. *Nature* **577**, 549–555 (2020).
58. Markowitz, J. et al. Patients with pancreatic adenocarcinoma exhibit elevated levels of myeloid-derived suppressor cells upon progression of disease. *Cancer Immunol. Immunother.* **64**, 149–159 (2015).
59. Stromnes, I. M. et al. Targeted depletion of an MDSC subset unmasks pancreatic ductal adenocarcinoma to adaptive immunity. *Gut* **63**, 1769–1781 (2014).
60. Di Mitri, D. et al. Tumor-infiltrating Gr-1$^+$ myeloid cells antagonize senescence in cancer. *Nature* **515**, 134–137 (2014).
61. Nywening, T. M. et al. Targeting both tumour-associated CXCR2$^+$ neutrophils and CCR2$^+$ macrophages disrupts myeloid recruitment and improves chemotherapeutic responses in pancreatic ductal adenocarcinoma. *Gut* **67**, 1112–1123 (2018).
62. Wherry, E. J. et al. Molecular signature of CD8$^+$ T cell exhaustion during chronic viral infection. *Immunity* **27**, 670–684 (2007).
63. Segal, N. H. et al. Results from an integrated safety analysis of urelumab, an agonist anti-CD137 monoclonal antibody. *Clin. Cancer Res.* **23**, 1929–1936 (2017).
64. Bartkowiak, T. et al. Activation of 4-1BB on liver myeloid cells triggers hepatitis via an Interleukin-27-dependent pathway. *Clin. Cancer Res.* **24**, 1138–1151 (2018).
65. Li, J. et al. Tumor cell-intrinsic factors underlie heterogeneity of immune cell infiltration and response to immunotherapy. *Immunity* **49**, 178–193 (2018).
66. Parra, E. R. et al. Validation of multiplex immunofluorescence panels using multispectral microscopy for immune-profiling of formalin-fixed and paraffin-embedded human tumor tissue. *Sci. Rep.* **7**, 13380 (2017).
67. Xie, P. et al. SuperCT: a supervised-learning network for enhanced characterization of single-cell transcriptomic profiles. *Nucleic Acids Res.* **47**, e48 (2019).
68. Lun, A. T. et al. EmptyDrops: distinguishing cells from empty droplets in droplet-based single-cell RNA sequencing data. *Genome Biol.* **20**, 63 (2019).
69. Young, M. D. & Behjati, S. SoupX removes ambient RNA contamination from droplet-based single-cell RNA sequencing data. *Gigascience* **9**, giaa151 (2020).
70. Butler, A., Hoffman, P., Smibert, P., Papalexi, E. & Satija, R. Integrating single-cell transcriptomic data across different conditions, technologies, and species. *Nat. Biotechnol.* **36**, 411–420 (2018).
71. Benjamini, Y. Discovering the false discovery rate. *J. R. Stat. Soc.* **72**, 405–416 (2010).

Acknowledgements

We thank the Small Animal Imaging Facility, Histology Core, Flow Cytometry and Cellular Imaging Core and Single Cell Genomics Core at the MD Anderson Cancer Center for assistance with these studies (NCI P30CA16672; CPRIT RP180684). We thank the members of the Multiplex Immunofluorescence and Image Analysis Laboratory in the Department of Translational Molecular Pathology for assistance with multiplex immunofluorescence and image analysis. We thank the Biospecimen Repository and Histopathology Service, Flow Cytometry and Cell Sorting Shared Resource, Biostatistics Shared Resource and Molecular Imaging Core at the Rutgers Cancer Institute of New Jersey (NCI P30CA072720). These studies were supported by NIH NCI P01 CA117969 (to R.A.D.), the Elsa Pardee Foundation Award, the Advanced Scholars Program, the Eleanor Russo Fund for Pancreatic Research, the Ralph A. Loveys Family Charitable Foundation, The Cultural & Charitable Club of Somerset Run and the New Jersey Health Foundation Award (to P.G.), NIH NCI R01CA240526 and R01CA236864 (to N.E.N.), NIH NCI R01CA231349 and 1R01CA258540 (to Y.A.W.) and NIH NCI R01CA220236 and P50CA221707, the Sheikh Khalifa Bin Zayed Foundation and MD Anderson's Pancreatic Cancer Moon Shot (to A.M.). We thank V. Kulkarni for assistance with figure preparation.

Author contributions

P.G. and R.A.D. conceived of and designed the study. P.G. performed most of the experiments and wrote the manuscript. A.S., E.S. and N.E.N. assisted with the design, performance and data analysis for the mouse scRNA-seq experiments. S.J. and X.S. assisted with the in vivo experiments and CyTOF. C.-J.W. and J.L. provided bioinformatics support for TCGA/ICGC and human scRNA-seq analysis. S.H.R., L.S.S. and E.P. assisted with the IHC and immunofluorescence of human PDAC specimens. P.H., H.Y., J.H., P. Dey and P. Deng assisted with the mouse colonies and in vivo experiments. D.Y.M. and J.A.Z. provided technical assistance with SX-682. D.J.S. assisted with manuscript editing, figure revisions and data review. M.K. and H.W. assisted with the procurement of human specimens. A.M. assisted with the procurement of human specimens and contributed expertise regarding PDAC and immunotherapy. K.C.-D. assisted with the flow cytometry experiments. D.M. assisted with the statistical analysis. All of the authors reviewed and edited the manuscript. Y.A.W. and R.A.D. supervised the study.

Competing interests

R.A.D. is a founder, advisor and/or director of Tvardi Therapeutics, Asylia Therapeutics, Stellanova Therapeutics, Nirogy Therapeutics and Sporos Bioventures. J.A.Z. is the President and Chief Executive Officer at Syntrix Pharmaceuticals. D.Y.M. is the Director of Medicinal Chemistry and Preclinical Development at Syntrix Pharmaceuticals. A.M. receives royalties from Cosmos Wisdom Biotechnology and Thrive Earlier Detection, an Exact Sciences company. A.M. is also a consultant for Freenome and Tezcat Biotechnology. The other authors declare no competing interests.

Additional information

Extended data is available for this paper at https://doi.org/10.1038/s43018-022-00500-z.

Supplementary information The online version contains supplementary material available at https://doi.org/10.1038/s43018-022-00500-z.

Correspondence and requests for materials should be addressed to Y. Alan Wang or Ronald A. DePinho.

[1]Department of Medical Oncology, Cancer Institute of New Jersey, Rutgers University, New Brunswick, NJ, USA. [2]Department of Gastrointestinal Medical Oncology, Division of Cancer Medicine, The University of Texas MD Anderson Cancer Center, Houston, TX, USA. [3]Department of Genetics, The University of Texas MD Anderson Cancer Center, Houston, TX, USA. [4]Department of Cancer Biology, The University of Texas MD Anderson Cancer Center, Houston, TX, USA. [5]Department of Genomic Medicine, The University of Texas MD Anderson Cancer Center, Houston, TX, USA. [6]Department of Translational Molecular Pathology, The University of Texas MD Anderson Cancer Center, Houston, TX, USA. [7]Department of Molecular and Cellular Oncology, The University of Texas MD Anderson Cancer Center, Houston, TX, USA. [8]Department of Immunology, Roswell Park Comprehensive Cancer Center, Buffalo, NY, USA. [9]Syntrix Pharmaceuticals, Auburn, WA, USA. [10]Department of Surgical Oncology, The University of Texas MD Anderson Cancer Center, Houston, TX, USA. [11]Department of Pathology, The University of Texas MD Anderson Cancer Center, Houston, TX, USA. [12]Department of Biostatistics, Cancer Institute of New Jersey, Rutgers University, New Brunswick, NJ, USA. [13]Department of Hematopoietic Biology and Malignancy, The University of Texas MD Anderson Cancer Center, Houston, TX, USA. [14]Brown Center for Immunotherapy, Indiana University School of Medicine, Indianapolis, IN, USA. [15]Department of Medicine, Indiana University School of Medicine, Indianapolis, IN, USA. [16]Department of Microbiology and Immunology, Indiana University School of Medicine, Indianapolis, IN, USA. [17]Indiana University Melvin and Bren Simon Comprehensive Cancer Center, Indianapolis, IN, USA. ✉e-mail: yaw@iu.edu; rdepinho@mdanderson.org

https://doi.org/10.1038/s43018-022-00500-z

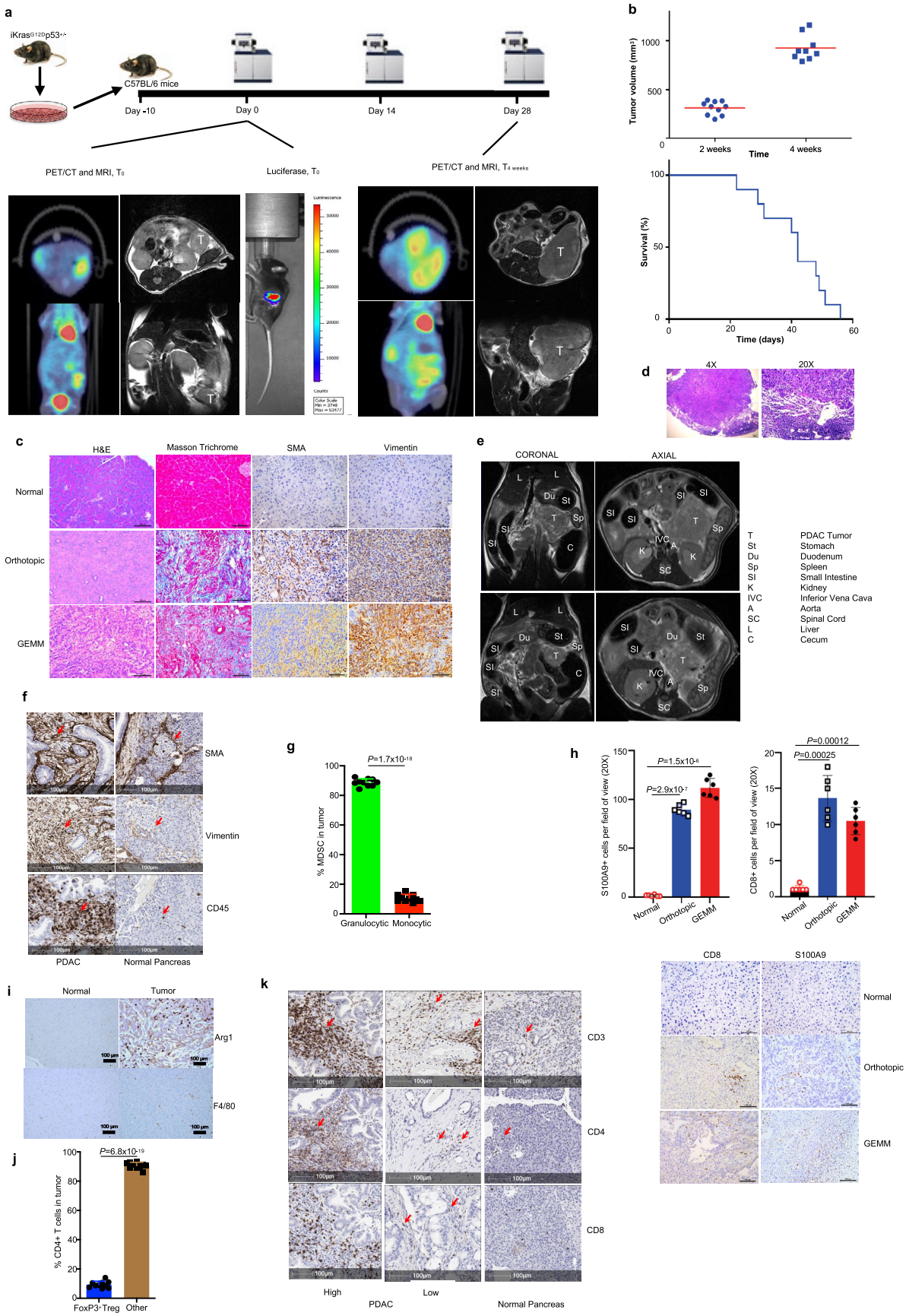

Extended Data Fig. 1 | See next page for caption.

https://doi.org/10.1038/s43018-022-00500-z

Extended Data Fig. 1 | Prominent infiltration of myeloid immunosuppressive cells in iKRAS tumors. A. PDAC tumor development in syngeneic mouse model with representative images of tumor detected by bioluminescence, PET/CT and MRI at indicated timepoints. **B**. Tumor volume measured by MRI at indicated timepoints (top) and Kaplan-Meier curve depicting overall survival (bottom) for untreated iKRAS tumor bearing mice (n = 10 mice). **C**. Representative images of normal pancreas, orthotopic and autochthonous (GEMM) iKRAS tumors with H&E, Masson Trichrome, smooth muscle actin (SMA) and vimentin staining. Scale bars: 100 μm. **D**. Representative H&E images of iKRAS tumors invading into adjacent lymph nodes (left = 4x magnification, right=20x magnification). **E**. Representative coronal and axial MRI images of iKRAS tumor invading into duodenum. **F**. Representative images of normal pancreas and human PDAC tumors with SMA, Vimentin and CD45 staining. Scale bars: 100 μm. Red arrow indicates positively stained cells. **G**. Percentage of granulocytic ($CD45^+CD11b^+Ly6G^+Ly6C^-$) and monocytic MDSCs ($CD45^+CD11b^+Ly6G^-Ly6C^+$) within syngeneic iKRAS tumors (n = 10 tumors) assessed by CyTOF at 4 weeks after initial tumor detection. Two-sided Student's *t*-test. **H**. Representative images (bottom) of normal pancreas, orthotopic and autochthonous (GEMM) iKRAS tumors with indicated staining. n = 6 biological replicates. Scale bars: 100 μm. The bar graph (top) shows quantification of each cell type as analyzed by IHC. Two-sided Student's *t*-test. **I**. Representative images of normal pancreas and orthotopic iKRAS tumors with indicated staining. Scale bars: 100 μm. **J**. Percentage of Treg ($CD45^+CD3^+TCR\beta^+CD4^+FoxP3^+$) among $CD4^+$ T cells within syngeneic iKRAS tumors (n = 10 tumors) assessed by CyTOF at 4 weeks after initial tumor detection. Two-sided Student's *t*-test. **K**. Representative images of normal pancreas and human PDAC tumors with indicated staining. Scale bars: 100 μm. Red arrow indicates positively stained cells. Data in **G**,**H**,**J** are presented as mean ± s.e.m.

https://doi.org/10.1038/s43018-022-00500-z

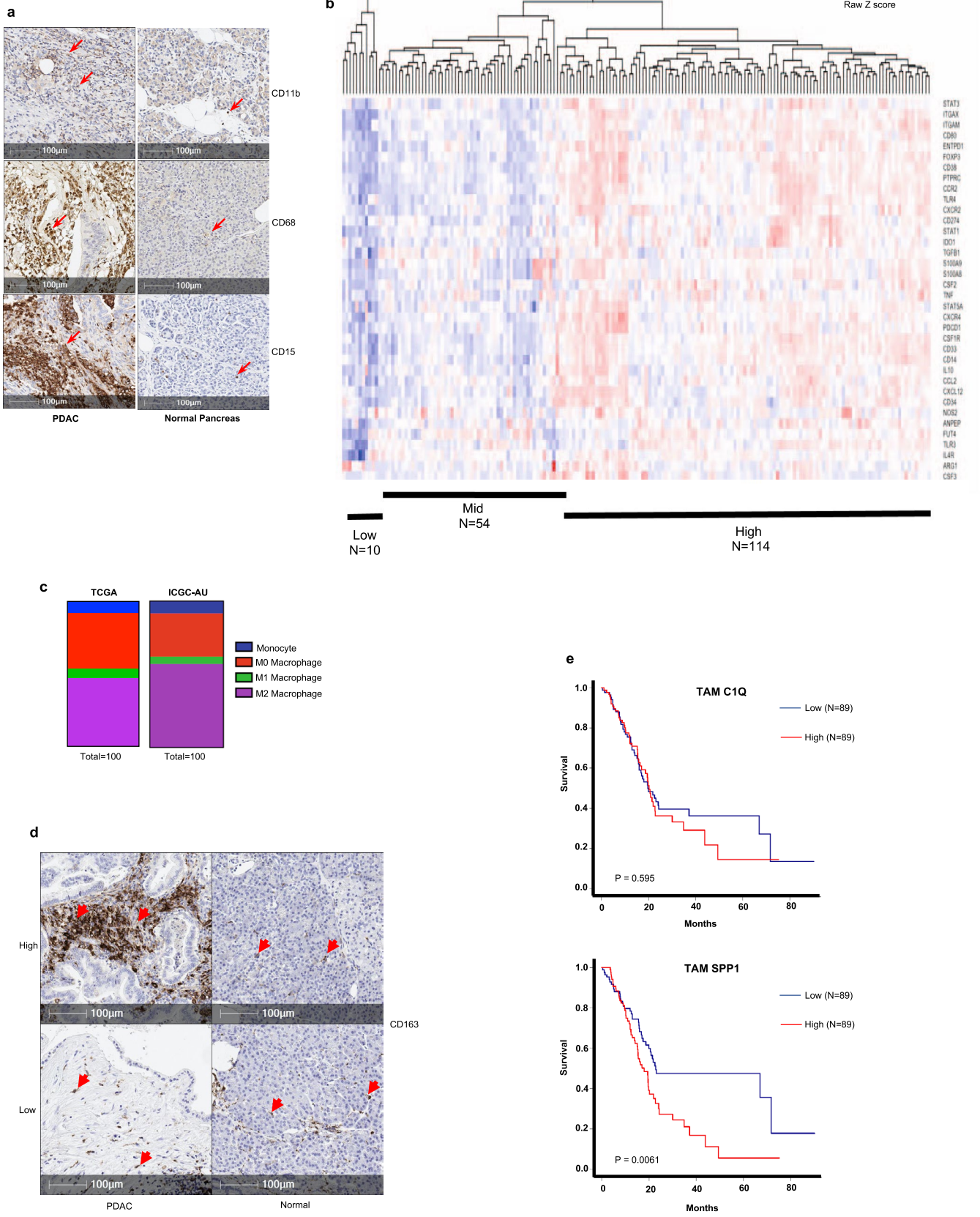

Extended Data Fig. 2 | See next page for caption.

https://doi.org/10.1038/s43018-022-00500-z

Extended Data Fig. 2 | Prominent infiltration of myeloid immunosuppressive cells in human PDAC tumors. A. Representative images of normal pancreas and human PDAC tumors with indicated staining. Scale bars: 100 µm. Red arrow indicates positively stained cells. **B**. Clustering of human TCGA PDAC samples (n = 178 patients) into MDSC-high, MDSC-low and MDSC-medium groups using a 39-gene MDSC signature[13]. **C**. CIBERSORTx quantification of monocyte/macrophage subset fraction in human PDAC samples; TCGA (n = 178 patients) and ICGC-AU (n = 92 patients). **D**. Representative images of normal pancreas and human PDAC tumors with indicated staining. Scale bars: 100 µm. Red arrow indicates positively stained cells. **E**. Kaplan-Meier plot depicting overall survival of TCGA PDAC patients (n = 178 patients) grouped by the gene expression signatures of $C1q^+$ TAM (top) and $Spp1^+$ TAM (bottom).

https://doi.org/10.1038/s43018-022-00500-z

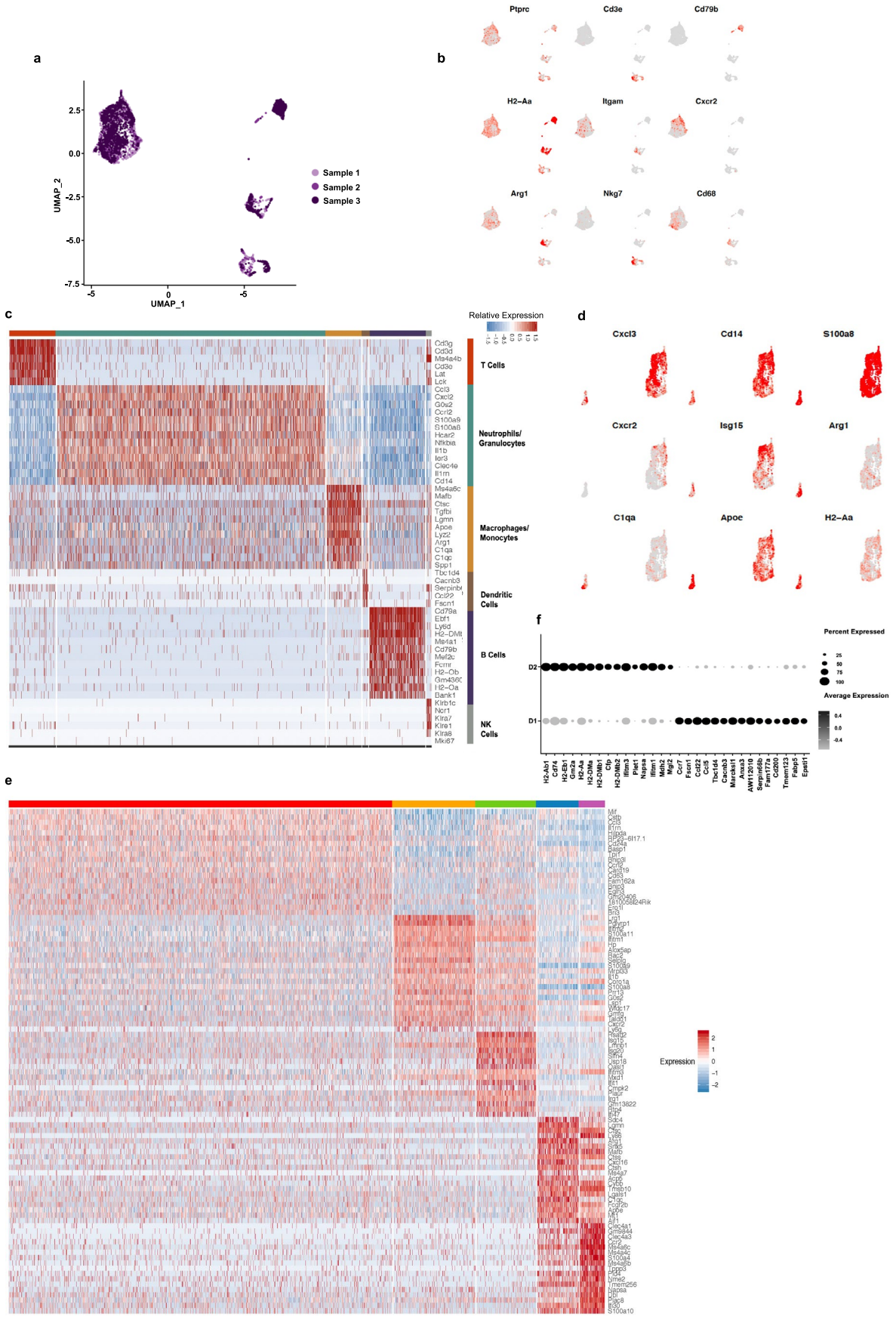

Extended Data Fig. 3 | See next page for caption.

https://doi.org/10.1038/s43018-022-00500-z

Extended Data Fig. 3 | Heterogeneity of myeloid cells in iKRAS PDAC tumors identified by single cell gene expression profiling. A. UMAP of all live $CD45^+$ cells used for scRNA-seq analysis of untreated iKRAS tumors (n = 4,080 cells). **B**. Representative genes and functional markers used for identification of immune cell clusters. **C**. Heatmap of six immune cell clusters with unique signature genes. **D**. Representative genes and functional markers used for identification of myeloid cell clusters. **E**. Heatmap of myeloid cell clusters with unique signature genes. **F**. Representative genes and functional markers used for identification of dendritic cell clusters.

https://doi.org/10.1038/s43018-022-00500-z

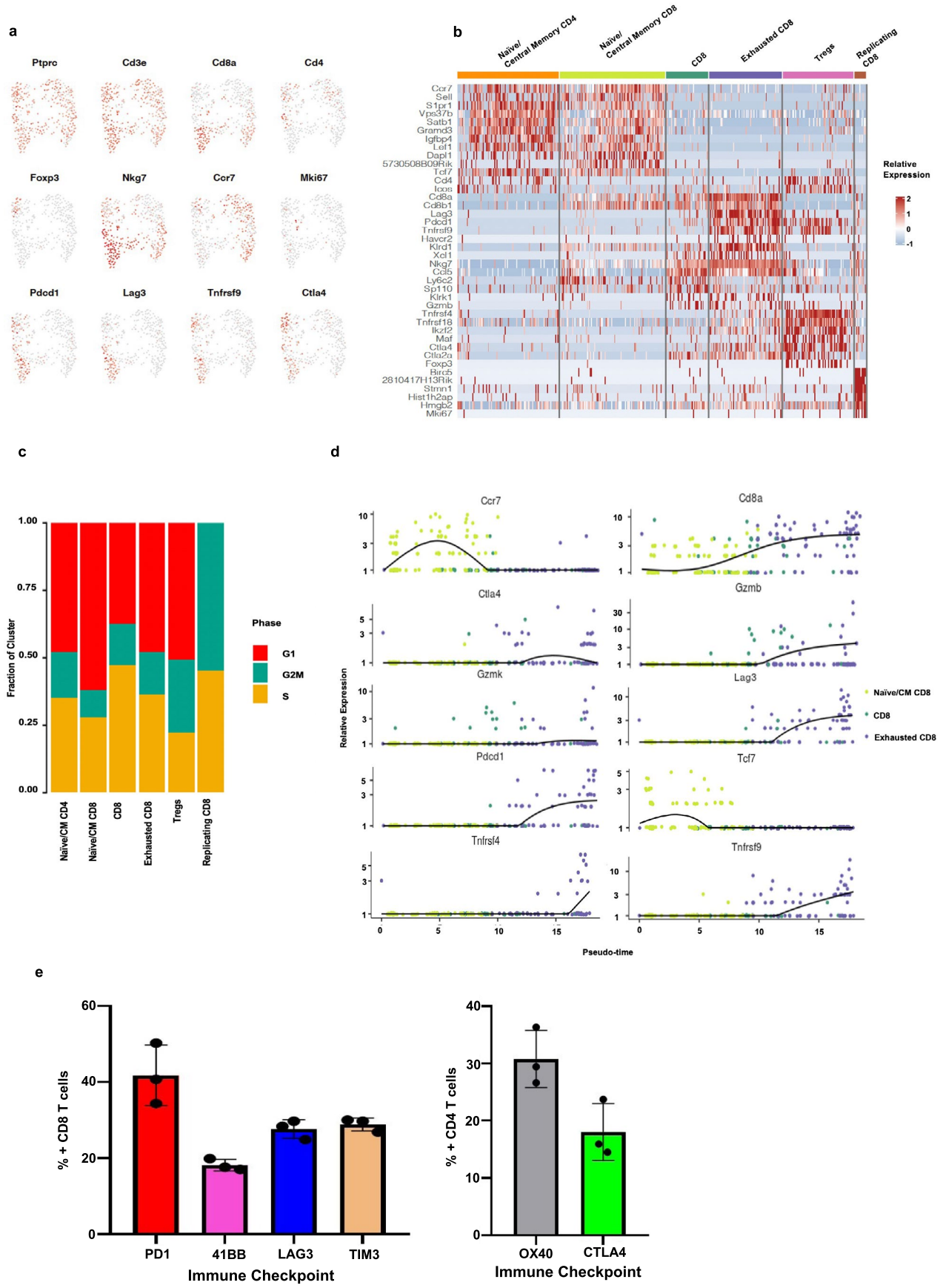

Extended Data Fig. 4 | See next page for caption.

https://doi.org/10.1038/s43018-022-00500-z

Extended Data Fig. 4 | Dysfunctional phenotype of T cells in iKRAS PDAC tumors identified by single cell gene expression profiling. A. Representative genes and functional markers used for identification of T cell clusters. **B**. Heatmap of two $CD4^+$ and four $CD8^+$ T cell clusters with unique signature genes. **C**. Cell cycle scoring for two $CD4^+$ and four $CD8^+$ T cell clusters. **D.** Relative expression of select genes in $CD8^+$ T cells as a function of pseudotime from Monocle2 inferred trajectory. Each point corresponds to a single cell, colored by $CD8^+$ T cell cluster. Lines represent average expression at that location in the trajectory. **E.** Quantification of immune checkpoint expression on infiltrating $CD4^+$ and $CD8^+$ T cells in iKRAS tumors (n = 3 biological replicates), assessed by flow cytometry and analyzed by FlowJo.

https://doi.org/10.1038/s43018-022-00500-z

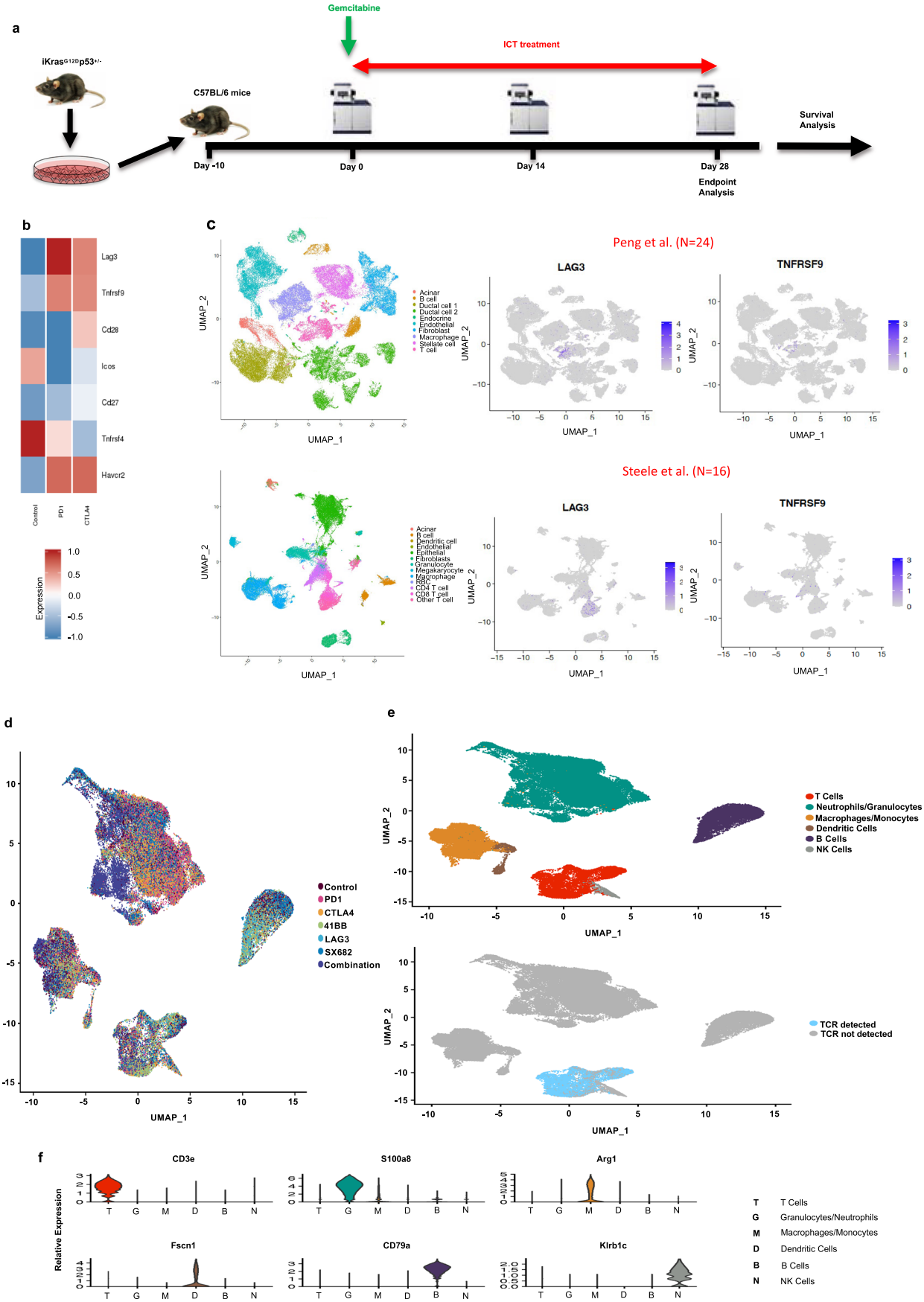

Extended Data Fig. 5 | See next page for caption.

https://doi.org/10.1038/s43018-022-00500-z

Extended Data Fig. 5 | Efficacy of immune checkpoint therapy (ICT) and treatment effects on immune microenvironment. A. Treatment schedule and monitoring procedures for preclinical trials to evaluate effect of ICT on iKRAS PDAC bearing mice. **B**. Heatmap of immune checkpoint expression on T cells after 4 week treatment with control, anti-PD1 or anti-CTLA4 antibody (n = 3 mice/ group). **C**. UMAP demonstrating cell types in single-cell RNA sequencing of human PDAC samples from Peng et al.[26] and Steele et al.[10] (left), and expression of LAG3 and 41BB (TNFRSF9) on T cells (right). **D**. UMAP of all live CD45$^+$ cells used for scRNA-seq analysis of iKRAS tumors treated with control, anti-PD1, anti-CTLA4, anti-41BB, anti-LAG3, SX-682 or combination (anti-LAG3 + anti-41BB + SX-682) treatment (n = 3 mice/group). **E**. UMAP projection of immune cell clusters (top) and cells with TCR detected (bottom). **F**. Violin plots displaying relative expression of representative genes and functional markers used for identification of immune cell clusters.

https://doi.org/10.1038/s43018-022-00500-z

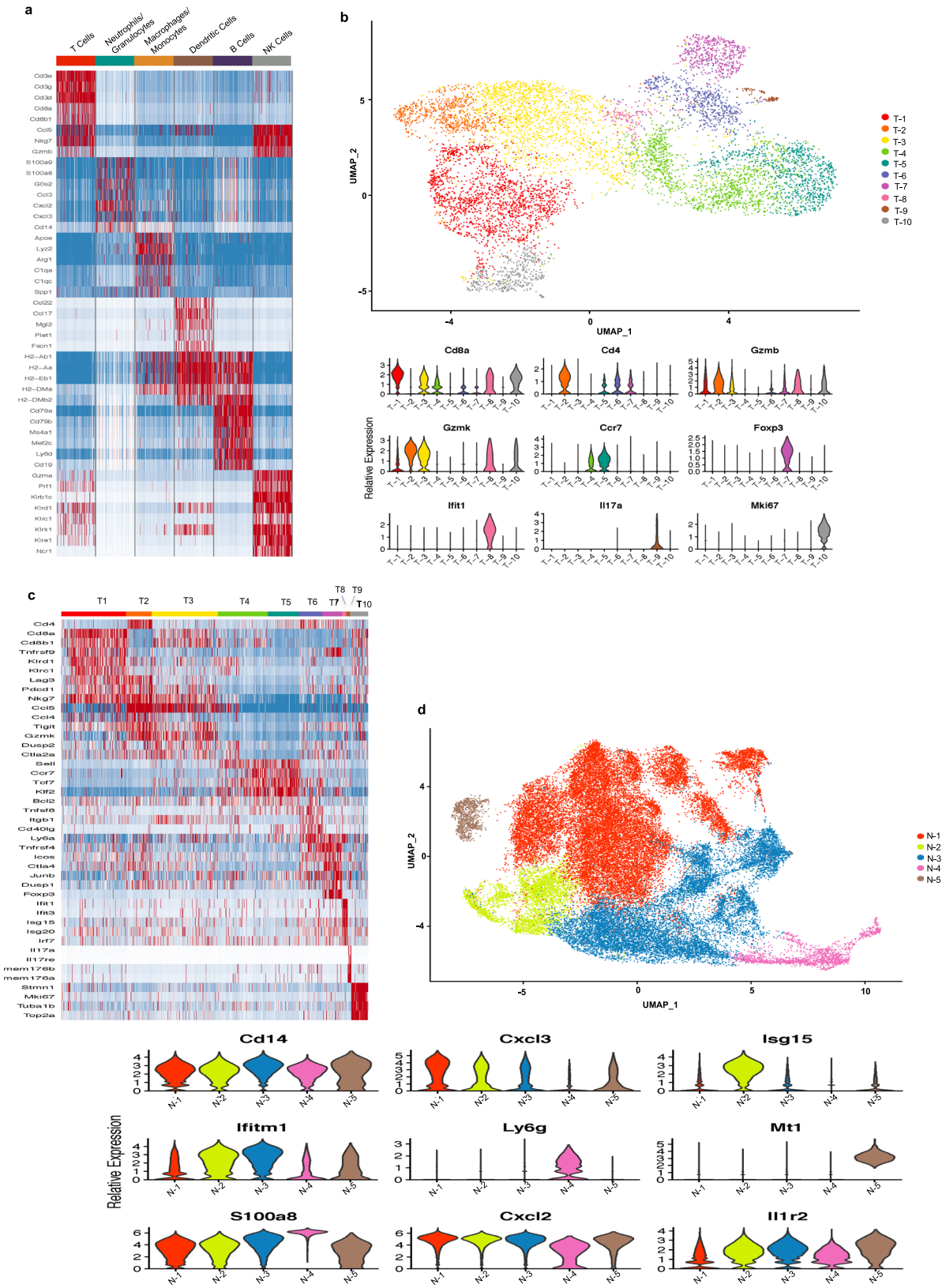

Extended Data Fig. 6 | Efficacy of immune checkpoint therapy (ICT) and treatment effects on immune microenvironment. A. Heatmap of six immune cell clusters with unique signature genes. **B.** UMAP projection of T cell clusters (top) and violin plots displaying relative expression of representative genes and functional markers used for identification of T cell clusters (bottom). **C.** Heatmap of ten T cell clusters with unique signature genes. **D.** UMAP projection of neutrophil/granulocyte clusters (top) and violin plots displaying relative expression of representative genes and functional markers used for identification of neutrophil/granulocyte clusters (bottom).

https://doi.org/10.1038/s43018-022-00500-z

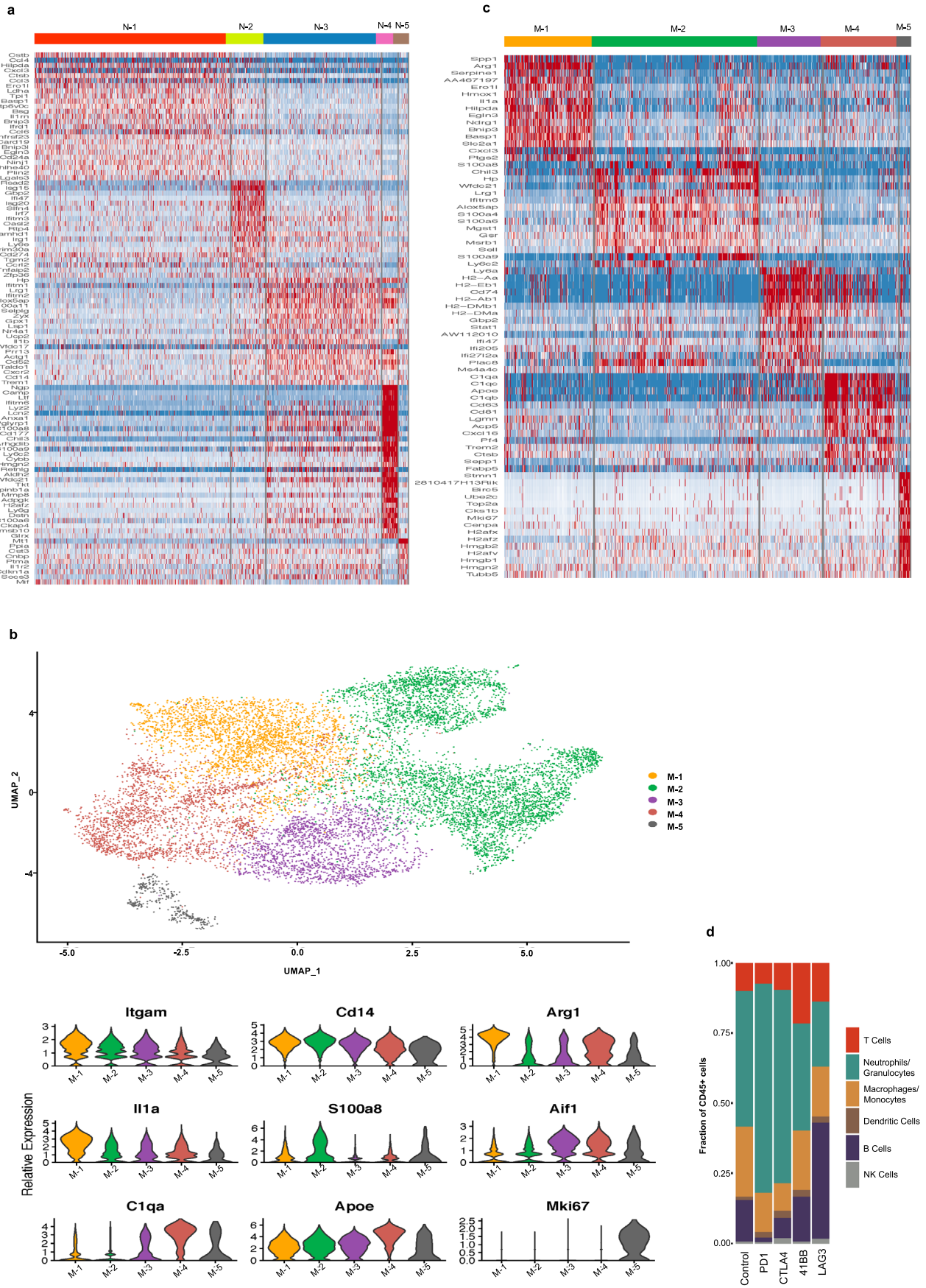

Extended Data Fig. 7 | See next page for caption.

https://doi.org/10.1038/s43018-022-00500-z

Extended Data Fig. 7 | Efficacy of immune checkpoint therapy (ICT) and treatment effects on immune microenvironment. A. Heatmap of five neutrophil/granulocyte clusters with unique signature genes. **B**. UMAP projection of monocyte/macrophage clusters (top) and violin plots displaying relative expression of representative genes and functional markers used for identification of monocyte/macrophage clusters (bottom). **C**. Heatmap of five monocyte/macrophage clusters with unique signature genes. **D**. Proportion of immune cell subtypes in single-cell sequencing analysis of established iKRAS tumors (tumor volume ~250mm^3 prior to treatment initiation) treated with control, anti-PD1, anti-CTLA4, anti-41BB or anti-LAG3 antibody for 4 weeks (n = 3 tumors/group).

https://doi.org/10.1038/s43018-022-00500-z

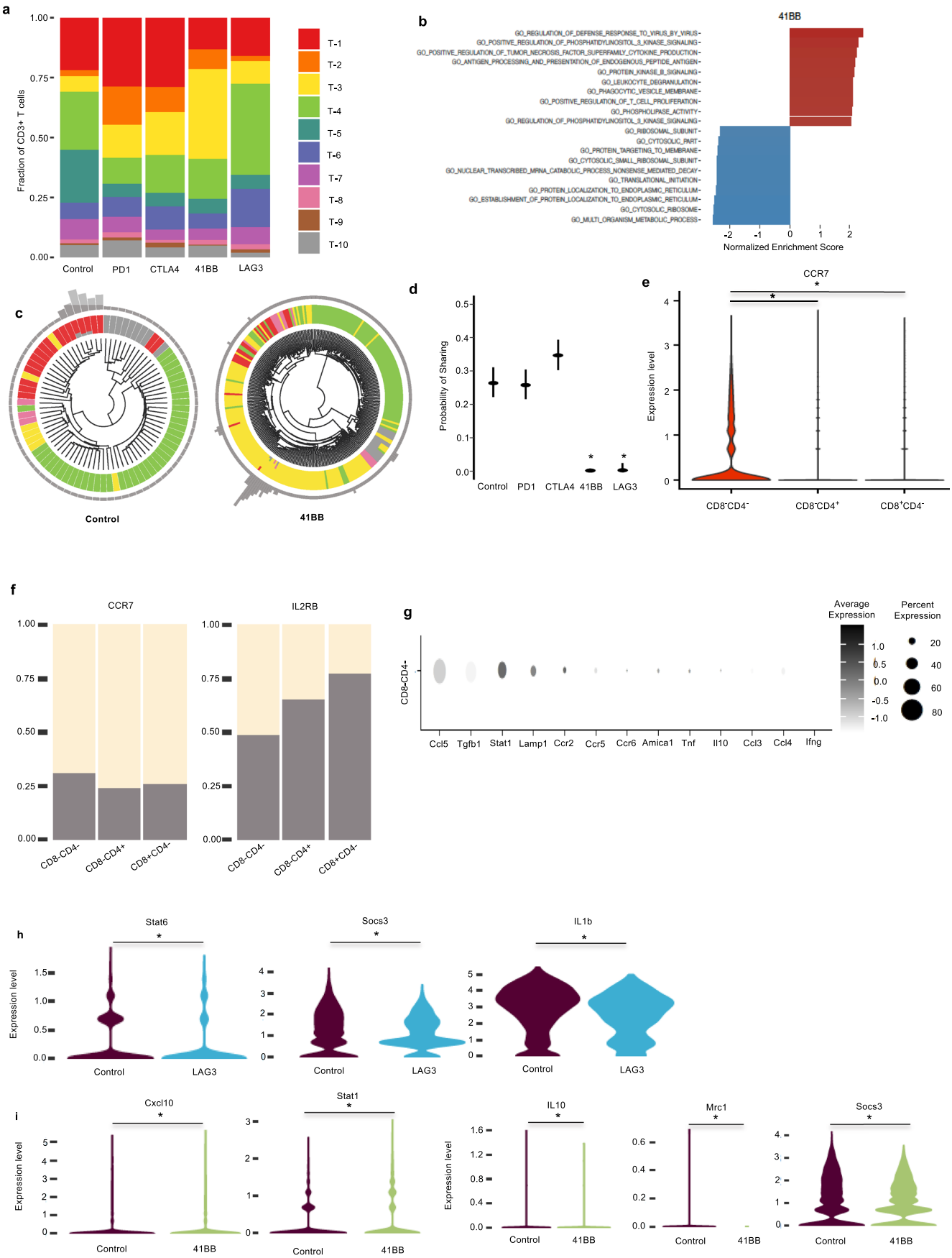

Extended Data Fig. 8 | See next page for caption.

https://doi.org/10.1038/s43018-022-00500-z

Extended Data Fig. 8 | Effects of immune checkpoint therapy (ICT) treatment on immune microenvironment. A. Proportion of T cell subtypes in scRNA-seq analysis of established iKRAS tumors (tumor volume ~250mm^3 prior to treatment initiation) treated with control, anti-PD1, anti-CTLA4, anti-41BB or anti-LAG3 antibody for 4 weeks (n = 3 tumors/group). **B**. Top gene ontologies from GSEA of differential expression in T cells from anti-41BB and control antibody treated mice (n = 3 mice/group). **C**. Circos plots of T cell receptor clonotype frequencies and expression states of CD8$^+$ T cells in iKRAS tumors after treatment with control (left) and anti-41BB antibody (right) for 4 weeks. Outer histogram is the frequency of each clonotype. Inner bars show the fraction of cells of particular clonotype in each expression state (colors correspond to the clusters in Extended Data Fig. 8a). Inner dendrograms are the hierarchical clustering of gene expression centroids for each clonotype. **D**. Multiple-testing corrected 95% binomial confidence intervals on the probability of a cell in each treatment group containing a TCR CD3R sequence which overlaps that of another cluster. (*p < 0.05) **E**. Violin plots showing CCR7 expression in CD4$^+$, CD8$^+$ and CD4$^-$CD8$^-$ T cells. (*p < 0.05 two-sided unpaired Wilcox test) **F**. Proportion of CD4$^+$, CD8$^+$ and CD4$^-$CD8$^-$ T cells with expression of CCR7 (left) and IL2Rβ (right). **G**. Expression of genes and functional markers on CD3$^+$CD4$^-$CD8$^-$ T cells. **H**. Violin plots showing expression of Stat6, Socs3 and Il1β among myeloid cells from control and anti-LAG3 antibody-treated tumors (n = 3 mice/group). (*p < 0.05 two-sided unpaired Wilcox test) **I**. Violin plots showing expression of Cxcl10, Stat1, Il10, Mrc1 and Socs3 among myeloid cells from control and anti-41BB antibody-treated tumors (n = 3 mice/group). (*p < 0.05 two-sided unpaired Wilcox test).

https://doi.org/10.1038/s43018-022-00500-z

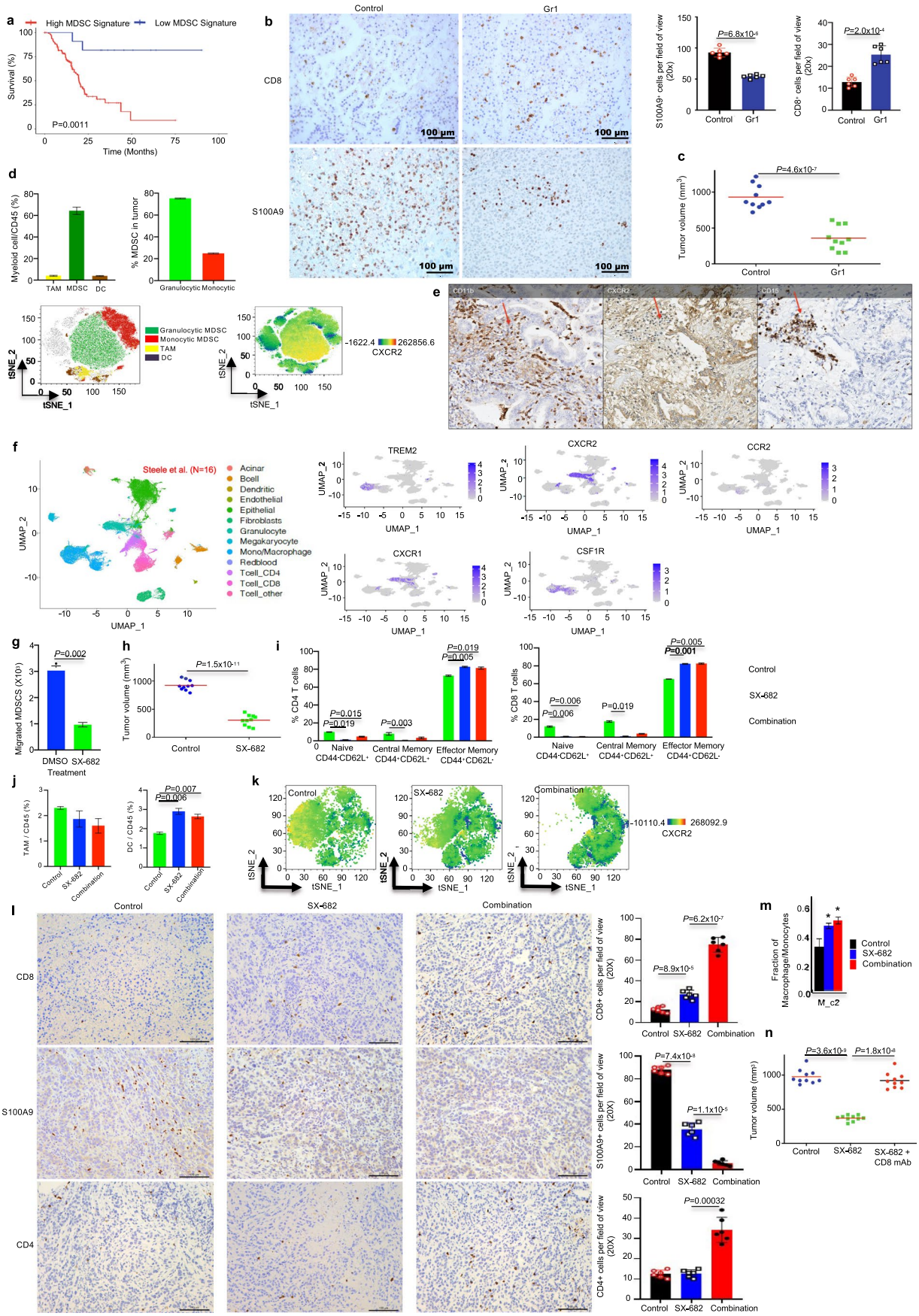

Extended Data Fig. 9 | See next page for caption.

https://doi.org/10.1038/s43018-022-00500-z

Extended Data Fig. 9 | Efficacy of targeted therapy directed against Cxcr1/2 and treatment effects on immune microenvironment. A. Kaplan-Meier plot depicting overall survival differences between patients with MDSC-high vs. MDSC-low signatures based on clustering of human TCGA PDAC samples (n = 178 patients) shown in Extended Data Fig. 2b. **B**. Representative images (left) of established iKRAS tumors treated with control and anti-Gr1 neutralizing antibody for 4 weeks with indicated staining. Scale bars: 100 µm. The bar graph (right) shows quantification of each cell type as analyzed by IHC. n = 6 biological replicates. Two-sided Student's *t*-test. **C**. Tumor volume after 4 weeks of treatment with control or anti-Gr1 neutralizing antibody in mice bearing established (tumor volume ~250mm^3 prior to treatment initiation) orthotopic iKRAS tumors (n = 10 mice/group). Two-sided Student's *t*-test. **D**. Expression of Cxcr2 on granulocytic MDSCs in untreated iKRAS tumors, assessed by flow cytometry and analyzed by FlowJo (n = 3 tumors). **E**. Representative images of human PDAC tumors with indicated staining. Scale bars: 100 µm. Red arrow indicates positively stained cells in the same area of a core specimen. **F**. UMAP demonstrating cell types in single-cell RNA sequencing of human PDAC samples from Steele et al.[10] with the expression of CXCR1 and CXCR2 on granulocytes/neutrophils and expression the of CSF1R, CCR2 and TREM2 on monocytes/macrophages. **G**. Migration of MDSCs toward conditioned medium from iKRAS tumor cells treated with control or SX-682 (n = 3 biological replicates). Student's *t*-test. **H**. Tumor volume after 4 weeks of treatment with control or SX-682 in mice bearing established orthotopic iKRAS tumors (tumor volume ~250mm^3 prior to treatment initiation) (n = 10 mice/group). Two-sided Student's *t*-test. **I**. Stratification of infiltrating CD4$^+$ and CD8$^+$ T cells as naive (CD44^{low}CD62L^{high}), central memory (CD44^{high}CD62L^{high}) and effector memory (CD44^{high}CD62L^{low}), in established iKRAS tumors (tumor volume ~250mm^3 prior to treatment initiation) treated with control, SX-682 or combination (anti-LAG3 + anti-41BB + SX-682) for 4 weeks assessed by flow cytometry and analyzed by FlowJo (n = 3 biological replicates). Two-sided Student's *t*-test. **J**. Quantification of total tumor associated macrophages (TAM) and dendritic cells (DC) in established iKRAS tumors (tumor volume ~250mm^3 prior to treatment initiation) treated with control, SX-682 or combination (anti-LAG3 + anti-41BB + SX-682) for 4 weeks assessed by flow cytometry and analyzed by FlowJo (n = 3 biological replicates). Two-sided Student's *t*-test. **K**. Expression of Cxcr2 on myeloid cells in established iKRAS tumors (tumor volume ~250mm^3 prior to treatment initiation) treated with control, SX-682 or combination (anti-LAG3 + anti-41BB + SX-682) for 4 weeks assessed by flow cytometry and analyzed by FlowJo (n = 3 biological replicates). **L**. Representative images (left) of control, SX-682 or combination (anti-LAG3 + anti-41BB + SX-682) treated iKRAS tumors with indicated staining. Scale bars: 100 µm. The bar graphs (right) show quantification of each cell type as analyzed by IHC. n = 6 biological replicates. Two-sided Student's *t*-test. **M**. Quantification of change in the proportion of cells in cluster M_c2 as a proportion of total monocyte/macrophage cells in scRNA-seq analysis of iKRAS tumors following treatment with control, SX-682 or combination (anti-LAG3 + anti-41BB + SX-682) for 4 weeks (n = 3 mice/group). (*p < 0.05 mixed effect model) **N**. Tumor volume of mice bearing established orthotopic iKRAS tumors (tumor volume ~250mm^3 prior to treatment initiation) treated with control, SX-682 or SX-682 with CD8 T cell depleting antibody (n = 10 mice/group). Two-sided Student's *t*-test. Data in **D**,**G**,**I**,**J**,**M** are presented as mean ± s.e.m.

https://doi.org/10.1038/s43018-022-00500-z

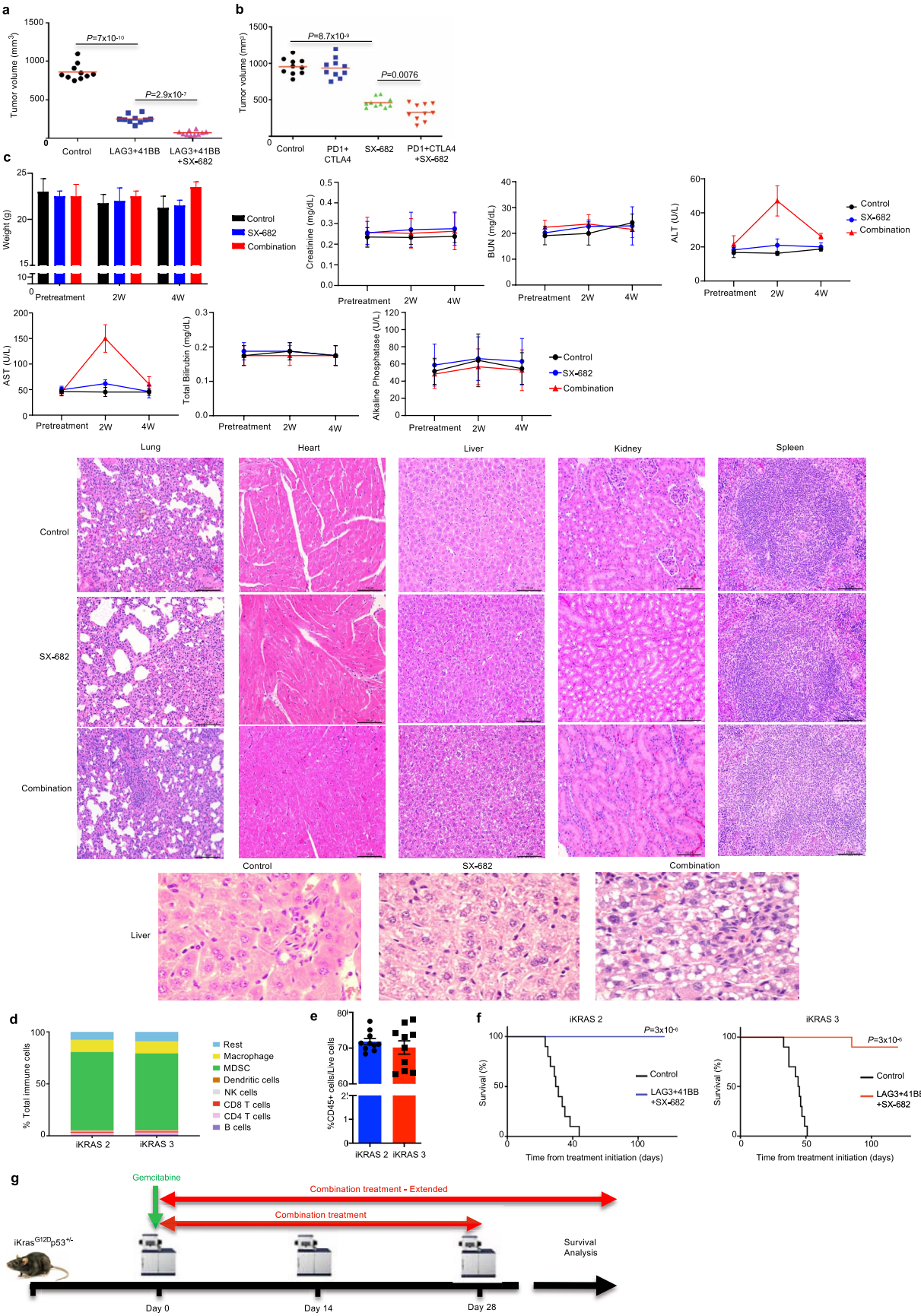

Extended Data Fig. 10 | See next page for caption.

https://doi.org/10.1038/s43018-022-00500-z

Extended Data Fig. 10 | Efficacy of ICT in combination with targeted therapy directed against Cxcr1/2 and treatment effects on immune microenvironment. A. Tumor volume of mice bearing established orthotopic iKRAS tumors (tumor volume ~250mm^3 prior to treatment initiation) treated with control or anti-LAG3 + anti-41BB antibodies or combination (anti-LAG3 + anti-41BB + SX-682) for 4 weeks (n = 10 mice/group). Two-sided Student's *t*-test. **B**. Tumor volume of mice bearing established orthotopic iKRAS tumors (tumor volume ~250mm^3 prior to treatment initiation) treated with control or anti-PD1 + anti-CTLA4 antibodies or SX-682 or anti-PD1 + anti-CTLA4 + SX-682 for 4 weeks (n = 10 mice/group). Two-sided Student's *t*-test. **C**. Body weight of mice (top left), before (pre-treatment), during (2 weeks) and after (4 weeks) treatment with control, SX-682 or combination (anti-LAG3 + anti-41BB + SX-682) for 4 weeks (n = 4 biological replicates). Mouse toxicity tests including creatinine, blood urea nitrogen (BUN), aspartate aminotransferase (AST), alanine aminotransferase (ALT), total bilirubin and alkaline phosphatase in the indicated treatment groups (n = 4 biological replicates). Representative images of H&E staining (middle) of the lung, heart, liver, kidney and spleen in the indicated treatment groups (n = 4 mice/group). Inset (bottom) shows representative H&E staining of liver tissues in the indicated treatment groups at higher magnification. **D**. CyTOF analysis of tumors from syngeneic iKRAS 2 and iKRAS 3 tumor bearing mice with equivalent tumor volume (~1000mm^3) (n = 10 tumors/group). **E**. Quantification of tumor infiltrating CD45$^+$ cells in syngeneic iKRAS 2 and iKRAS 3 tumors with equivalent tumor volume (~1000mm^3) assessed by CyTOF (n = 10 tumors/group). **F**. Overall survival of mice bearing established orthotopic iKRAS 2 and iKRAS 3 tumors (tumor volume ~250mm^3 prior to treatment initiation) treated with control or anti-LAG3 + anti-41BB + SX-682 for 4 weeks (n = 10 mice/group). Statistical differences were identified by Kaplan-Meier with log-rank test. **G**. Treatment schedule and monitoring procedures for preclinical trial to evaluate overall survival of mice bearing established autochthonous iKRAS tumors (tumor volume ~250mm^3 prior to treatment initiation) treated with control or anti-PD1 + anti-CTLA4 antibodies or anti-LAG3 + anti-41BB antibodies or SX-682 or combination (anti-LAG3 + anti-41BB + SX-682) (n = 10 mice/group). Animals in the 'extended' treatment group received treatment with the combination regimen for 6 months or until death. Data in **E** are presented as mean ± s.e.m.

nature portfolio

Corresponding author(s): Ronald A. DePinho

Last updated by author(s): Nov 11, 2022

Reporting Summary

Nature Portfolio wishes to improve the reproducibility of the work that we publish. This form provides structure for consistency and transparency in reporting. For further information on Nature Portfolio policies, see our Editorial Policies and the Editorial Policy Checklist.

Statistics

For all statistical analyses, confirm that the following items are present in the figure legend, table legend, main text, or Methods section.

n/a	Confirmed
☐	☒ The exact sample size (*n*) for each experimental group/condition, given as a discrete number and unit of measurement
☐	☒ A statement on whether measurements were taken from distinct samples or whether the same sample was measured repeatedly
☐	☒ The statistical test(s) used AND whether they are one- or two-sided *Only common tests should be described solely by name; describe more complex techniques in the Methods section.*
☒	☐ A description of all covariates tested
☒	☐ A description of any assumptions or corrections, such as tests of normality and adjustment for multiple comparisons
☐	☒ A full description of the statistical parameters including central tendency (e.g. means) or other basic estimates (e.g. regression coefficient) AND variation (e.g. standard deviation) or associated estimates of uncertainty (e.g. confidence intervals)
☐	☒ For null hypothesis testing, the test statistic (e.g. *F*, *t*, *r*) with confidence intervals, effect sizes, degrees of freedom and *P* value noted *Give P values as exact values whenever suitable.*
☒	☐ For Bayesian analysis, information on the choice of priors and Markov chain Monte Carlo settings
☒	☐ For hierarchical and complex designs, identification of the appropriate level for tests and full reporting of outcomes
☒	☐ Estimates of effect sizes (e.g. Cohen's *d*, Pearson's *r*), indicating how they were calculated

Our web collection on statistics for biologists contains articles on many of the points above.

Software and code

Policy information about availability of computer code

Data collection

COMPUTATIONAL ANALYSIS OF HUMAN PDAC TCGA, ICGC AND SINGLE-CELL RNA SEQUENCING DATA

For TCGA GSEA analysis, the TCGA PDAC mRNA dataset, gene mutations and clinical survival was downloaded from the TCGA website. For ICGC GSEA analysis, the ICGC PDAC AU mRNA dataset, gene mutations and clinical survival was downloaded from the ICGC data portal. Two human PDAC single-cell RNA sequencing cohorts were used from Peng et al. [27] and Steele et al. [10].

SINGLE-CELL RNA SEQUENCING, TRANSCRIPTOMIC AND T CELL RECEPTOR ANALYSIS OF MOUSE TUMORS

Flow cytometry to isolate live, CD45+ cells was performed using standard protocol as noted above on FACSAria Fusion sorter (Becton Dickinson) and analyzed with FlowJo software version 10 (Tree Star). Live, CD45+ cells were processed with the 10X Genomics Chromium platform, with the 5′ V(D)J solution chemistry per the manufacturer's protocol. T cell receptor sequences were enriched with the primers listed below, and the resulting libraries were pooled and sequenced 150bp PE on the Illumina Miseq with the V2 300cycle kit. Single cell transcriptome libraries were pooled and sequenced 26bp-91bp PE on the Novaseq S2 to a targeted depth of 100,000 reads per cell. Raw sequencing data were processed through the 10X Genomics cellranger pipeline version 2.1.0 and then analyzed in R.

10X_forward_1 5′-AATGATACGGCGACCACCGAGATCTACACTCTTTCCCTACACGACGCTC-3′
10X_forward_2 5′-AATGATACGGCGACCACCGAGATCT-3′
TRAC_inner_mouse 5′-ACACAGCAGGTTCTGGGTTCT-3′
TRAC_outer_mouse 5′-TGAAGCTTGTCTGGTTGCTC-3′
TRBC_inner_mouse 5′-TGATGGCTCAAACAAGGAGAC-3′
TRBC_outer_mouse 5′-TGTGCCAGAAGGTAGCAGAGAC-3′

Data analysis

COMPUTATIONAL ANALYSIS OF HUMAN PDAC TCGA, ICGC AND SINGLE-CELL RNA SEQUENCING DATA

For analysis of human PDAC data, we utilized a 39 gene human MDSC signature, which was described previously [19]. The gene expression data of 178 TCGA PDAC samples were clustered using the 39 MDSC genes into MDSC-high, MDSC-low, and MDSC-medium (distance between pairs of samples was measured by Manhattan distance, and clustering was then performed using complete-linkage hierarchical clustering). Similarly normalized gene expression data from PDAC TCGA (178 samples) or ICGC-AU (92 samples) were used to infer the relative proportions of infiltrating immune cells using the CIBERSORTx algorithm which was described previously [17]. Estimated fractions of each immune cell subset were related to survival using univariate Cox regression. Two human PDAC single-cell RNA sequencing cohorts were used from Peng et al. [27] and Steele et al. [10]. For Peng et al. cohort, original cell type annotations of single-cell RNA clusters were used. For Steele et al. cohort, data were processed and clustered according to the R scripts from the original paper. UMAP clusters were further annotated using rSuperCT algorithm [67]. Expression of selected marker genes were compared among different cell types. All data processing and analysis were implemented in R 4.0.5 environment and Seurat package version 4.0.1.

SINGLE-CELL RNA SEQUENCING, TRANSCRIPTOMIC AND T CELL RECEPTOR ANALYSIS OF MOUSE TUMORS

Raw sequencing data were processed through the 10X Genomics cellranger pipeline version 2.1.0 and then analyzed in R. Cells were detected using the DropletUtils package [68] with an FDR of 0.01, and barcode swapped counts were removed using swappedDrops. Supernatant RNA contamination was filtered using the package SoupX [69]. Data were then processed using the Seurat package [70]. Cells with a mitochondrial gene percentage greater than 15% were filtered, and samples were corrected for batch effects by aligning the first 35 canonical correlations using the MultiCCA function. Cells were clustered with SNN. Differences in cluster fractions were assessed by the significance of treatment as a fixed effect in a binomial mixture model (glmer in the lme4 R package) with replicate included as a random effect. Pseudotime analysis was performed using the Monocle2 package per the recommended workflow [35]. To determine the lineage of each individual T cell in the PDAC tumors after the various ICT treatments, we designed primers for the mouse α and β TCR locus and performed targeted PCR on the 10X genomics single-cell 5′ cDNA product (Supplementary Table 4). From the TCR product library, we assembled the full-length TCR α and β sequences. Raw TCR sequencing data were processed through the 10X Genomics cellranger vdj pipeline version 2.1.0. Clonotypes where only an α or β chain were detected, but exactly matched arCDR3 nucleotide sequence from an α-β paired clonotype were combined into the paired clonotype for further analysis.

STATISTICAL ANALYSIS

Changes in average relative expression or expression of gene signature scores in scRNA-seq analyses was performed by two-sided unpaired Wilcox test. For single cell populations, differences in cluster fractions were assessed by the significance of treatment as a fixed effect in a binomial mixture model (glmer in the lme4 R package) with sample replicate included as a random effect.

For manuscripts utilizing custom algorithms or software that are central to the research but not yet described in published literature, software must be made available to editors and reviewers. We strongly encourage code deposition in a community repository (e.g. GitHub). See the Nature Portfolio guidelines for submitting code & software for further information.

Data

Policy information about availability of data

All manuscripts must include a data availability statement. This statement should provide the following information, where applicable:

- Accession codes, unique identifiers, or web links for publicly available datasets
- A description of any restrictions on data availability
- For clinical datasets or third party data, please ensure that the statement adheres to our policy

Source data for main figures and supplementary figures are provided in the online version of this paper. Murine single-cell RNA sequencing and TCR sequencing data supporting the findings of this study have been deposited on Sequence Read Archive (SRA) under BioProject accession code PRJNA496487. Human PDAC genomic data were derived from the TCGA Research Network [http://cancergenome.nih.gov] and ICGC Research Network [https://dcc.icgc.org]. Human PDAC single-cell RNA sequencing data were derived from [CRA001160, https://ngdc.cncb.ac.cn/gsa/browse/CRA001160] and [GSE155698, https://www.ncbi.nlm.nih.gov/geo/query/acc.cgi?acc=GSE155698]. All other data are available from the corresponding authors upon reasonable request.

Human research participants

Policy information about studies involving human research participants and Sex and Gender in Research.

Reporting on sex and gender	Clinicopathologic information including age, race, gender, neoadjuvant therapy, type of surgery and pathologic staging are listed in Supplementary Table 1 for human PDAC CyTOF analyses.
Population characteristics	See above
Recruitment	Human PDAC samples were obtained from MD Anderson's Tissue Biobank. PDAC patients were recruited by surgeons performing pancreatectomy at MDACC.
Ethics oversight	Human studies were approved by MD Anderson's Institutional Review Board (IRB), and informed consent was obtained from all subjects under IRB protocol LAB05-0854.

Note that full information on the approval of the study protocol must also be provided in the manuscript.

Field-specific reporting

Please select the one below that is the best fit for your research. If you are not sure, read the appropriate sections before making your selection.

☒ Life sciences ☐ Behavioural & social sciences ☐ Ecological, evolutionary & environmental sciences

For a reference copy of the document with all sections, see nature.com/documents/nr-reporting-summary-flat.pdf

Life sciences study design

All studies must disclose on these points even when the disclosure is negative.

Sample size	No statistical method was used to predetermine sample size. The animal cohort sizes for the study were estimated based on previous experience using similar mouse models that showed significance [8, 16, 19]. Total of at least ten mice were used for each treatment arm, which is sufficient to detect meaningful differences based on prior experience with similar experiments. The exact number of mice per group are listed in the figure legend.
Data exclusions	No data were excluded from the analysis.
Replication	Total of atleast ten mice were used for each treatment arm. The exact number of mice per group are listed in the figure legend.
Randomization	In vivo preclinical trial experiments involving treatment of mice with orthotopic or GEM iKRAS tumors were randomized and investigators were blinded to allocation during experiments and outcome assessment. For in vitro experiments, all samples were analyzed equally with no subsampling; therefore, there was no requirement for randomization.
Blinding	Investigators were blinded to allocation and outcome assessment for in vivo preclinical trial experiments involving treatment of mice with orthotopic or GEM iKRAS tumors.

Reporting for specific materials, systems and methods

We require information from authors about some types of materials, experimental systems and methods used in many studies. Here, indicate whether each material, system or method listed is relevant to your study. If you are not sure if a list item applies to your research, read the appropriate section before selecting a response.

Materials & experimental systems

n/a	Involved in the study
☐	☒ Antibodies
☐	☒ Eukaryotic cell lines
☒	☐ Palaeontology and archaeology
☐	☒ Animals and other organisms
☒	☐ Clinical data
☒	☐ Dual use research of concern

Methods

n/a	Involved in the study
☒	☐ ChIP-seq
☐	☒ Flow cytometry
☒	☐ MRI-based neuroimaging

Antibodies

Antibodies used

FLOW CYTOMETRY:
CD45 (clone 104, 109822, 1:100), CD62L (clone MEL-14, 104445, 1:100), FOXP3 (clone MF-14, 126404, 1:100), TIM3 (B8.2C12, 134008, 1:100), CTLA4 (clone UC10-4B9, 106313, 1:100), PD-1 (clone 29F.1A12, 135221, 1:100), LAG3 (clone C9B7W, 125212, 1:100), OX40 (clone OX-86, 119418, 1:100), Ki-67 (clone 16A8, 652410, 1:100), CD11b (clone M1/70, 101226, 1:50), Ly6C (clone HK1.4, 128012, 1:100), Ly6G (clone 1A8, 127641, 1:100), F4/80 (clone BM8, 123131, 1:200), CD206 (clone C068C2, 141719, 1:100) from Biolegend; EpCAM (clone G8.8, 740281, 1:100), CD44 (clone IM7, 612799, 1:100), 41BB (clone 1AH2, 740364, 1:200), CD11c (clone HL3, 612797, 1:200), MHC II (clone 2G9, 743876, 1:100), CXCR2 (clone V48-2310, 747811, 1:100) from BD; CD8 (clone 53-6.7, 35-0081-82, 1:100) from Thermofisher; CD4 (clone RM4-5, 25-0042-U100, 1:100) from Tonbo.

MULTIPLEX IF:
Panel 1: pancytokeratin (clone AE1/AE3, M351501-2, 1:300, Dako), CD3 (IS503, 1:100, Dako), CD8 (clone C8/144B, MS-457s, 1:300, Thermo Fisher Scientific), CD45RO (clone UCHL1, PA0146, no dilution [ready to use], CST), granzyme B (clone 11F1, PA0291, no diluation [ready to use], CST); Panel 2: pancytokeratin (clone AE1/AE3, M351501-2, 1:25, Dako), CD3 (IS503, 1:100, Dako), LAG3 (clone D2G4O, 15372, 1:200, CST); Panel 3: pancytokeratin (clone AE1/AE3, M351501-2, 1:50, Dako), CD11b (clone ERP13344, 133357, 1:6000, Abcam), CD14 (clone SP192, M4920, 1:300, Abcam), CD66b (clone G10F5, 305102, 1:100, Biolegend), CD33 (clone PWS44, NCL-L-CD33, 1:50, Leica), and CD68 (clone PG-M1, M087601-2, 1:50, Dako); Panel 4: CD3 (IS503, 1:100, Dako), CD137 (clone D2Z4Y, 34594, 1:25, CST).

IHC:

Primary antibodies for mouse tissue staining included: CD4 (CST 25229, 1:100), CD8 (CST 98941, 1:500), SMA (Abcam 5694, 1:200), Vimentin (CST 5741, 1:500), S100A9 (Proteintech 14226-1-AP, 1:500), F4/80 (CST 70076S, 1:500), Arginase-1 (CST 93668S, 1:200). Primary antibodies for human tissue staining included: CD3 (Dako A0452), CD4 (Cell Marque 104R-16, 1:100), CD8 (ThermoScientific MS-457, 1:50), CD45 (Dako M0701), CD163 (Leica NCL-L-CD163), CD15 (BD Biosciences 347420, 1:100), CD68 (Dako M0814), CXCR2 (Abcam 225732, 1:2000), CD11b (Abcam 133357, 1:4000), SMA (Leica NCL-L-SMA), Vimentin (Dako M0725).

IN VIVO ANTIBODIES:
Anti-PD1 (clone RMP1-14, BioXCell, BE0146), anti-CTLA4 (clone 9H10, BioXCell, BE0131), anti-TIM3 (clone RMT3-23, BioXCell, BE0115), anti-OX40 (clone OX-86, BioXCell, BE0031), anti-41BB (clone LOB12.3, BioXCell, BE0169), anti-LAG3 (clone C9B7W, BioXCell, BE0174), anti-CD8 (clone 2.43, BioXCell, BE0061) and anti-Gr1 (clone RB6-8C5, BioXCell, BE0075),

Antibodies used for human and mouse CyTOF analysis are listed in Supplementary Table 2.

Validation

All antibodies were validated extensively by the provider, used in multiple studies previously. Validation references for each antibody are available on manufacturer website. Catalog numbers and manufacturer are listed above. Extra validation was performed by comparing expression in internal controls (known negative populations).

Eukaryotic cell lines

Policy information about cell lines and Sex and Gender in Research

Cell line source(s)	iKRAS (p48Cre; tetO_LSL-KrasG12D; ROSA_rtTA; p53L/+) syngeneic cell lines were generated by the DePinho lab and have been described previously [8].
Authentication	Cell lines were not authenticated.
Mycoplasma contamination	All cell lines were tested for Mycoplasma and found to be negative within 3 months of performing experiments.
Commonly misidentified lines (See ICLAC register)	No commonly misidentified lines were used in this study.

Animals and other research organisms

Policy information about studies involving animals; ARRIVE guidelines recommended for reporting animal research, and Sex and Gender in Research

Laboratory animals	iKRAS (p48Cre; tetO_LSL-KrasG12D; ROSA_rtTA; p53L/+) genetically engineered mice were described previously and were backcrossed to the C57BL/6 background for more than eight generations to achieve a pure B6 mouse to generate syngeneic cell lines [8]. Female and male mice were administered doxy water starting at 4 weeks of age to activate transgenic KRASG12D expression to generate autochthonous tumors. For orthotopic pancreas transplantation, C57BL/6 female or male mice aged 5-7 weeks (Jackson Labs) were utilized. All mice were closely monitored by authors, animal facility technicians (during treatments and experiments) and by veterinary scientists responsible for animal welfare. Mice were maintained with a 12h light-dark cycle, under controlled temperature and humidity (18-23C and 40-60% respectively) and given ad libitum access to standard diet and water.
Wild animals	No wild animals were used in the study.
Reporting on sex	Female and male C57BL/6 mice aged 5-7 weeks (Jackson Labs) were utilized for orthotopic pancreas transplantation studies. Female and male mice were administered doxy water starting at 4 weeks of age to activate transgenic KRASG12D expression to generate autochthonous tumors.
Field-collected samples	No field-collected samples were used in the study.
Ethics oversight	All animal work performed in this study was approved by MD Anderson (protocol #00001039 Utilize Mouse Models to Study Pancreatic Cancer) and Rutgers (protocol #202000076 Mouse Studies for Pancreatic Cancer) Institutional Animal Care and Use Committees.

Note that full information on the approval of the study protocol must also be provided in the manuscript.

Flow Cytometry

Plots

Confirm that:

☒ The axis labels state the marker and fluorochrome used (e.g. CD4-FITC).

☒ The axis scales are clearly visible. Include numbers along axes only for bottom left plot of group (a 'group' is an analysis of identical markers).

☒ All plots are contour plots with outliers or pseudocolor plots.

☒ A numerical value for number of cells or percentage (with statistics) is provided.

Methodology

Sample preparation	Tumor cells were isolated from iKRAS tumors using the Mouse Tumor Dissociation Kit (Miltenyi Biotec). Single cells were isolated from tumors using standard protocol and as described previously [16, 19]. All isolated cells were depleted of erythrocytes by hypotonic lysis. To assess cell viability, cells were incubated with Ghost dye violet (Tonbo Biosciences) for 15 minutes in dark and then stained with indicated antibodies for 30 minutes on ice prior to FACS analysis. Fluorochrome-conjugated antibodies were as listed above. For FOXP3 staining, cells were fixed and permeabilized (eBioscience FOXP3/ Transcription Factor Staining Buffer Set) and stained with FOXP3. All samples were acquired with the FACSAria Fusion sorter (Becton Dickinson) and analyzed with FlowJo software version 10 (Tree Star).
Instrument	FACSAria Fusion sorter (Becton Dickinson)
Software	FlowJo software version 10 (TreeStar)
Cell population abundance	Cell population abundance has been outlined in the manuscript and figures.
Gating strategy	Gating strategy has been outlined in the manuscript and figures.

☒ Tick this box to confirm that a figure exemplifying the gating strategy is provided in the Supplementary Information.